

Surface wave tomography across the Sorgenfrei–Tornquist Zone, SW Scandinavia, using ambient noise and earthquake data

Andreas Köhler,¹ Valérie Maupin¹ and Niels Balling²

¹Department of Geosciences, University of Oslo, P.O. Box 1047, 0316 Oslo, Norway. E-mail: andreas.kohler@geo.uio.no

²Department of Geoscience, Aarhus University, Høegh-Guldbergs Gade 2, 8000, Aarhus C, Denmark

Accepted 2015 July 14. Received 2015 May 26; in original form 2015 January 19

SUMMARY

We produce a *S*-wave velocity model of the crust and upper mantle around the Sorgenfrei–Tornquist Zone, southern Scandinavia, by analysing ambient seismic noise and earthquake recordings on temporary and permanent regional network stations. In a first step, we perform tomographical inversion of surface wave dispersion data from seismic noise to obtain Rayleigh and Love wave phase-velocity maps from 3 to about 30 s period. Local dispersion curves are then combined with regionally averaged surface wave velocities from earthquake data measured between 15 and about 100 s period. Dispersion curves are jointly inverted for a 3-D model of the *S*-wave velocity and radial velocity anisotropy by using a combined Monte Carlo and linearized inversion approach. Results reveal significant crustal as well as uppermost mantle velocity variations at all depth levels. Upper crustal structural variations are mainly controlled by the thick sedimentary Danish Basin with both low *S*-wave velocities and high anisotropy. Despite of the known limited capability of surface wave inversion to constrain interface depths and model parameter trade-offs, obtained Moho depths are in good agreement with previous studies in the region. Marked crustal thinning is clearly revealed beneath the Danish Basin with a narrow transition to the thicker crust in Swedish shield areas. Despite very different crustal and morphological structures, Denmark and southern Norway both have similar well-defined upper-mantle low-velocity zones, interpreted as asthenosphere, starting a depth of about 100 km. Compared with southern Sweden, showing high upper-mantle velocities, characteristic for shields, velocities are reduced by 0.30–0.40 km s⁻¹ (6–8 per cent) at the depth levels of 140–200 km and radial anisotropy of 2–4 per cent is observed. Our study confirms the importance of the Sorgenfrei–Tornquist Zone, as a very deep structural boundary, separating old, thick, cratonic Baltica lithosphere in southern Sweden from reworked and attenuated Baltica lithosphere in Denmark and southern Norway.

Key words: Interferometry; Surface waves and free oscillations; Seismic anisotropy; Seismic tomography; Dynamics of lithosphere and mantle; Crustal structure.

1 INTRODUCTION

This study region of southwestern Scandinavia (Figs 1 and 2) displays significant geological-tectonic and morphological differences and marked contrasts in crustal and upper-mantle structure. It contains the tectonic transition from old Precambrian Baltic Shield in southern Sweden to the much younger Phanerozoic deep basins in the Danish area. Tectonic units in southern Norway include shield units and Scandinavian Caledonides with regions of high topography (southern Scandes) in contrast to the lowlands of Denmark and most of southern Sweden.

Previous seismological studies have demonstrated significant contrast in both crustal and upper-mantle structure across southern Scandinavia (see, Maupin *et al.* 2013, for a recent review). Crustal

thickness varies markedly across the Kattegat Sea, from thick crust in southern Sweden, of up to more than 45 km, to the 30 km thick crust of the Danish Basin (e.g. Eugeno-S Working Group 1988; Thybo 2001; Alinaghi *et al.* 2003; Sandrin & Thybo 2008). Relatively thick crust (about 40 km) is also observed in southern Norway beneath areas of high topography compared to about 30 km in coastal areas (Svenningsen *et al.* 2007; Stratford *et al.* 2009). High-resolution *P*-wave traveltimes tomography studies (Medhus *et al.* 2012) covering the whole of our study region, and similar *S*-wave tomography studies focused on southern Norway (Wawerzinek *et al.* 2013), have revealed marked seismic velocity contrasts in the upper mantle with high seismic velocity to great depth beneath southern Sweden and lower velocities beneath Denmark and most of southern Norway. Information from surface wave studies have previously

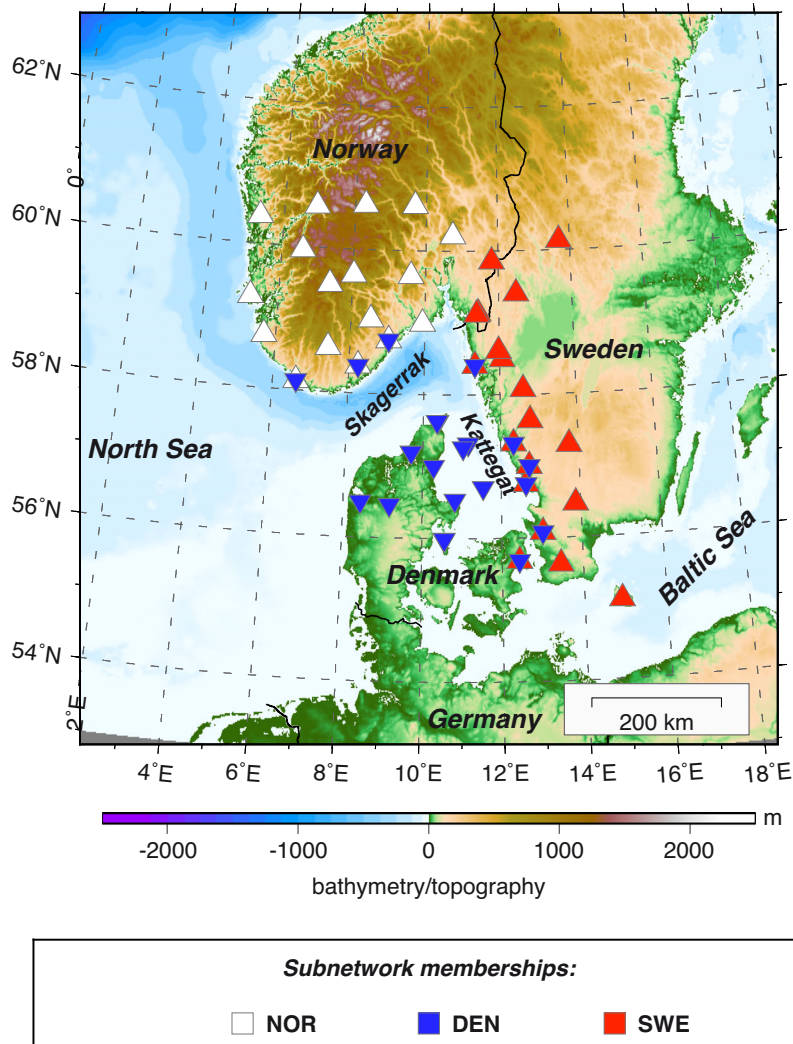


Figure 1. Location of the study area of southwestern Scandinavia and distribution of seismological stations in the three subnetworks NOR (white), DEN (blue) and SWE (yellow). Note that some stations belong to two subnetworks.

been presented by Pedersen *et al.* (1994) (for southernmost Norway and Jutland, Denmark), Cotte *et al.* (2002) (southern Sweden, Denmark and northernmost Germany) and recently by Maupin (2011) and Köhler *et al.* (2012) (southern Norway), also demonstrating the existences of significant deep velocity contrasts. The most recent *S*-wave velocity model obtained from surface wave tomography in southern Norway (Köhler *et al.* 2012) shows small-amplitude velocity anomalies in the upper crust that can be related to surface geology and lateral variation of crustal thickness in agreement with previous studies. Furthermore, the transition from a slow lithospheric upper mantle underneath southern Norway to a fast mantle toward Sweden was confirmed in that study. We lack however a complete model to the south across the Skagerrak, Kattegat and the Sorgenfrei–Tornquist Zone (Figs 1 and 2), with good lateral resolution at crustal and shallow mantle depths that could give us more information about the relation between deep regional structure and surface geology.

In this study, Rayleigh and Love wave phase velocities from 3 to about 100 s period are analysed and inverted providing information on both crustal and upper-mantle structure in terms of *S*-wave velocity distribution and anisotropy. We analyse surface waves using ambient seismic noise and earthquake record-

ings on a temporary regional network of seismological stations (Fig. 1).

Ambient seismic noise cross-correlation allows to extract short-period surface wave dispersion data from empirical Green's functions (Shapiro & Campillo 2004; Sabra *et al.* 2005). Combining seismic noise and earthquake analysis for inversion of local shear wave velocity depth profiles provides a continuous sensitivity from shallow crustal to deeper mantle structures (Yao *et al.* 2008; Yang *et al.* 2011), and moreover allows to analyse radial anisotropy in the crust if Rayleigh and Love wave observations are present (Moschetti *et al.* 2010a; Guo *et al.* 2012; Köhler *et al.* 2012). This study for the first time combines earthquake and seismic noise recordings with consistent analyses of data covering the main structural provinces across the southwestern part of Scandinavia including the northern part of the prominent Tornquist Zone.

2 TECTONIC SETTING

Three main tectonic units are represented in our study area; Precambrian Baltic Shield (southern Sweden and parts of southern Norway), Scandinavian Caledonides (mainly southern Norway) and Danish Basin covering most of Denmark (Fig. 2). The

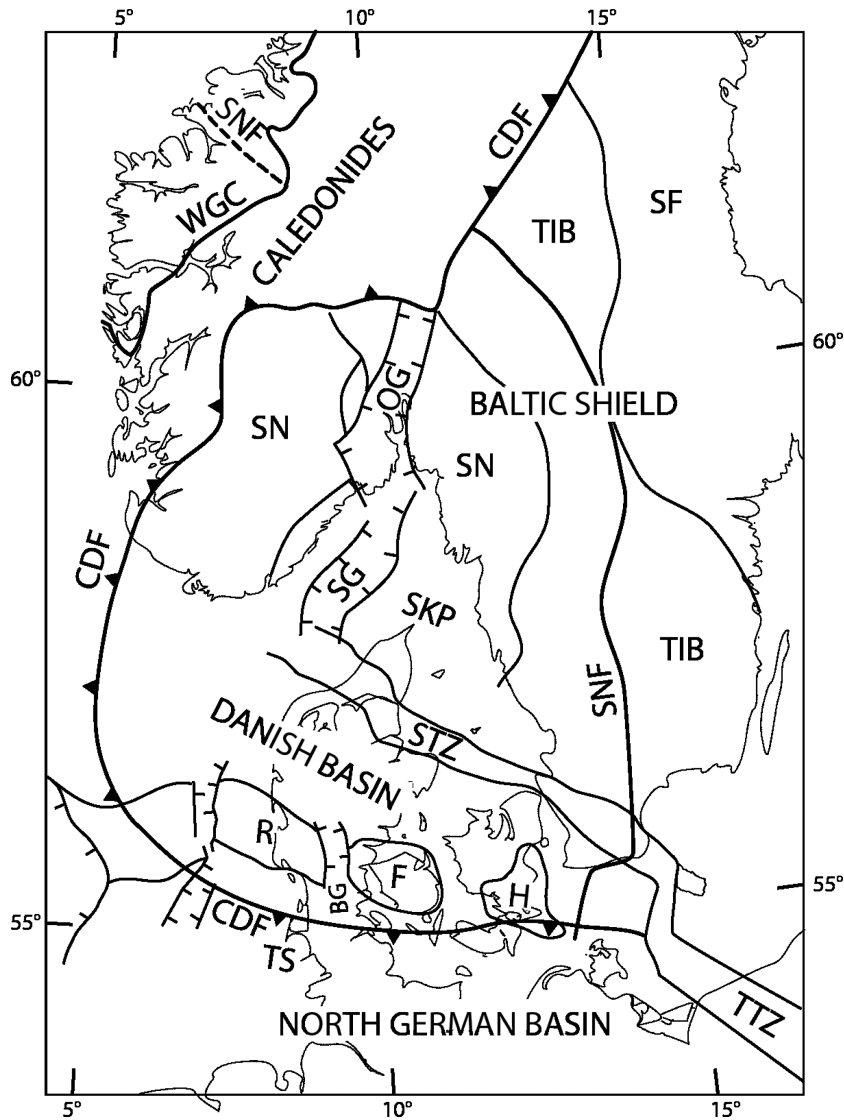


Figure 2. Structural outline with main tectonic units of the study area. CDF, Caledonian front; OG, Oslo Graben; RFH, Ringkøbing-Fyn High; SG, Skagerrak Graben; SF, Svecofennian; SN, Sveconorwegian; SNF, Sveconorwegian front; STZ, Sorgenfrei-Tornquist Zone; TIB, Trans-Scandinavian Igneous Belt; TS, Thor Suture; TTZ, Teisseyre-Tornquist Zone; WGC, Western Gneiss Complex.

oldest orogeny represented is the Svecofennian with generally juvenile rocks formed around 1.9 to 1.8 Ga ago. Rocks from this composite orogeny (Lahtinen *et al.* 2008) cover large areas in the central and southern parts of the Baltic Shield, and are found in the easternmost part of our region. Following this orogeny, crustal growth continued, generally from east to west (in present day coordinates), by formation of the subduction related 1.85–1.65 Ga Transscandinavian Igneous Belt (Högdahl *et al.* 2004), to the west of which about 1.65–1.5 Ga old tectonic units are found, including the Idefjorden and Telemarkia terranes (Bingen *et al.* 2008a). Most of these Palaeo- and Mesoproterozoic crustal units were extensively reworked by the 1.14–0.9 Ga old Sveconorwegian orogeny (Bingen *et al.* 2008b). Precambrian crust beneath the Danish area was also affected by this event, which resulted from continent–continent collision between palaeocontinent Baltica and another major plate.

The Late Ordovician to Early Devonian Caledonian orogeny was caused by a three-plate collision between Baltica, Laurentia and Avalonia (Cocks & Torsvik 2006). Around 440 Ma, the micro-

continent Avalonia, which was rifted off from northernmost Gondwana, was docking with Baltica, soon to be followed by collision of Baltica/Avalonia with Laurentia around 430–410 Ma (Roberts 2003; Torsvik & Cocks 2005) creating the Scandinavian Caledonides. Collision followed after closure of two oceans, the Tornquist Ocean between Baltica and Avalonia and the Iapetus Ocean between Baltica and Laurentia (with Greenland). Pronounced thrust systems were formed with generally east-vergent structures in Scandinavia and west-vergent in Greenland (Gee *et al.* 2008). Extensional collapse and erosion have led to exposure of Precambrian crystalline crust in the Western Gneiss Complex in southwestern Norway. To the south, the Caledonian orogeny resulted in the presence of Caledonian/Avalonian crust in the southernmost part of Denmark, northern Germany and in the North Sea. These units are mostly concealed beneath deep sedimentary sequences. Areas of present high topography (the southern Scandes Mountains) are not restricted to Caledonian units, but extend further south into our study area (Figs 1 and 2). A debate persists on whether Scandinavian high topography is old (e.g. basically a remnant of the mountain building

processes of the Caledonian orogeny as argued by Nielsen *et al.* (2009, 2010) or geologically much younger (e.g. Japsen & Chalmers 2000; Gabrielsen *et al.* 2005; Chalmers *et al.* 2010; Green *et al.* 2013); see also discussion in Maupin *et al.* (2013).

The Late Carboniferous to Early Permian was a period of pronounced magmatic activity in the North Sea and adjacent areas (Heeremans & Faleide 2004) and large regional sedimentary basins were initiated including the Danish and North German Basins. Heating and lithospheric extension seem to play a dominating role in basin formation and evolution (*cf.* Frederiksen *et al.* 2001). Up to about 10 km of sedimentary sequences are deposited in the Danish Basin. In southern Norway, and extending into the Skagerrak Sea, the Oslo Graben system was formed by rifting and intrusion of igneous rocks at around 300 Ma (e.g. Torsvik *et al.* 2008). Other tectonic events which may have had an impact on deep structures and seismic velocities in the investigated region are Late Palaeozoic and Mesozoic rifting offshore Norway and the Cenozoic opening of the North Atlantic Ocean.

3 INSTRUMENTATION AND DATA

The studied area is centred on the Skagerrak and Kattegat area, at the border of southern Norway, southern Sweden and northeastern Denmark (Fig. 1), combining data from 17 seismic broad-band receivers of the temporary MAGNUS network (Weidle *et al.* 2010) to the north with data from five temporary stations in Sweden to the east and nine temporary stations in Denmark (CALAS array, Medhus *et al.* 2012). Furthermore, 17 permanent stations in the entire area are used. Most instruments, including the permanent stations, have corner periods of 120 s (STS-2, CMG-3T). Half of the temporary sites in Denmark and Sweden as well as three stations of the permanent Swedish network have 30 s instruments (CMG-6T, CMG-40T). We correct all data for instrument response to allow the processing of periods longer than the corner period (i.e. 30–100 s). The MAGNUS stations were recording between 2006 September and 2008 June while the other temporary stations were recording over shorter time periods since late 2007 or early 2008. We can only use data recorded simultaneously at several stations in case of earthquake data. Interstation phase velocities can be measured from ambient noise as soon as two stations record simultaneously. Therefore, the length of data used varies for different station pairs.

4 PHASE-VELOCITY MAPS FROM AMBIENT SEISMIC NOISE

Phase-velocities in the shorter period range are obtained by analysis of ambient noise. We follow broadly the processing described in Köhler *et al.* (2011, 2012), where an ambient noise tomography is performed in southern Norway, to the north of our study area.

4.1 Measurement of phase-velocities

Seismic records are preprocessed by applying instrument correction, bandpass filtering (2–100 s), time domain normalization and prewhitening of the spectrum in the frequency domain (Bensen *et al.* 2007; Köhler *et al.* 2011). We compute cross-spectra for each station pair using the vertical and tangential seismogram component of 70 per cent overlapping and 27-min long time windows (see Seats *et al.* 2012, for a discussion of time window length and overlap). This window is sufficiently long to resolve traveltimes differences of surface waves for the longest interstation distances in this study. We

transform the cross-spectra back into time domain to obtain noise cross-correlation functions (NCFs). NCFs are stacked over the time period of available data for the corresponding station pair (examples of retrieved NCFs are shown in Fig. A1).

For pairs including stations of the MAGNUS network and/or the permanent installations KONO, HFC, BSD, COP and MUD, the available time period is 18–20 months. Lack of overlap due to short operation periods of temporary deployments in Denmark and Sweden reduced the data length available for stacking for corresponding station pairs to 4–13 months. Furthermore, stations of the permanent Swedish network started operating at different times in late 2007 and early 2008. An average record length of about 100 days can be used for pairs including BJU, LUN and DEL. For the rest of the Swedish network sites used here, 10 months of data are available.

We measure phase-velocity dispersion curves for each station pair from the vertical and transverse cross-correlation stacks by applying time–frequency analysis (FTAN, Levshin *et al.* 1989; Ritzwoller & Levshin 1998). We apply FTAN interactively which helps us to select only reasonable group velocity dispersion curves (Köhler *et al.* 2011). At this stage, station pairs having bad time–frequency images resulting from too short stack lengths are rejected manually (examples of FTAN images are given in Figs A2 and A3). Phase velocities are obtained from phase measurements at the point in time given by the (previously picked and measured) group velocity (Bensen *et al.* 2007). Subsequently, phase-velocity is corrected interactively for the phase ambiguity (multiple of 2π) as well as for a phase factor of $\pi/4$ that arise from interference of a homogeneous noise source distribution (Lin *et al.* 2008). In a few cases, no measurements were available for periods >20 s and at the same time interstation distance was too large to resolve the phase ambiguity with high confidence (see Lin *et al.* 2008). The station pair was then rejected to avoid a possible wrong phase correction.

Since separation between fundamental and higher modes is good in the considered period band for Rayleigh wave group velocities, we ensure that only the fundamental mode phase-velocity dispersion curve is measured. Love wave group velocities may exhibit mode overlapping for periods <10 s. If indications for higher modes are present during interactive FTAN processing, we reject the corresponding period range for Love waves. In case of unrecognized mixture of group velocity modes, the phase measurements will not result in a realistic and stable phase-velocity dispersion curve, and measurements are rejected as well. We are able to measure phase velocities within the period range of 3–30 s. For most station pairs, however, in particular those including sites in Denmark, we do not obtain reliable measurements below 5 s for Rayleigh waves, and 7 s for Love waves. We think that this is mostly due to more attenuation in the thick sediments of the Danish upper crust (Figs 2 and 3). The upper limit for many station pairs is about 20 s for Rayleigh and 12 s for Love waves, what can be explained by lack of a sufficiently long stacking intervals required for long-period NCFs.

Phase measurements may be disturbed by the inhomogeneity and variability of the noise source distribution (Lin *et al.* 2008). In our previous work further north in southern Norway (Köhler *et al.* 2011), we prepared three month long stacks and used them to assess the directionality and temporal variation of the noise field. This also provided a measure of the standard deviation of the phase velocities (Köhler *et al.* 2012). We showed that despite of significant seasonal variation in the noise source distribution, low standard deviation and stable dispersion curves can be obtained. Due to short stacking windows for a lot of station pairs, we cannot do the same analysis here for all station pairs. Therefore, quality control of the phase

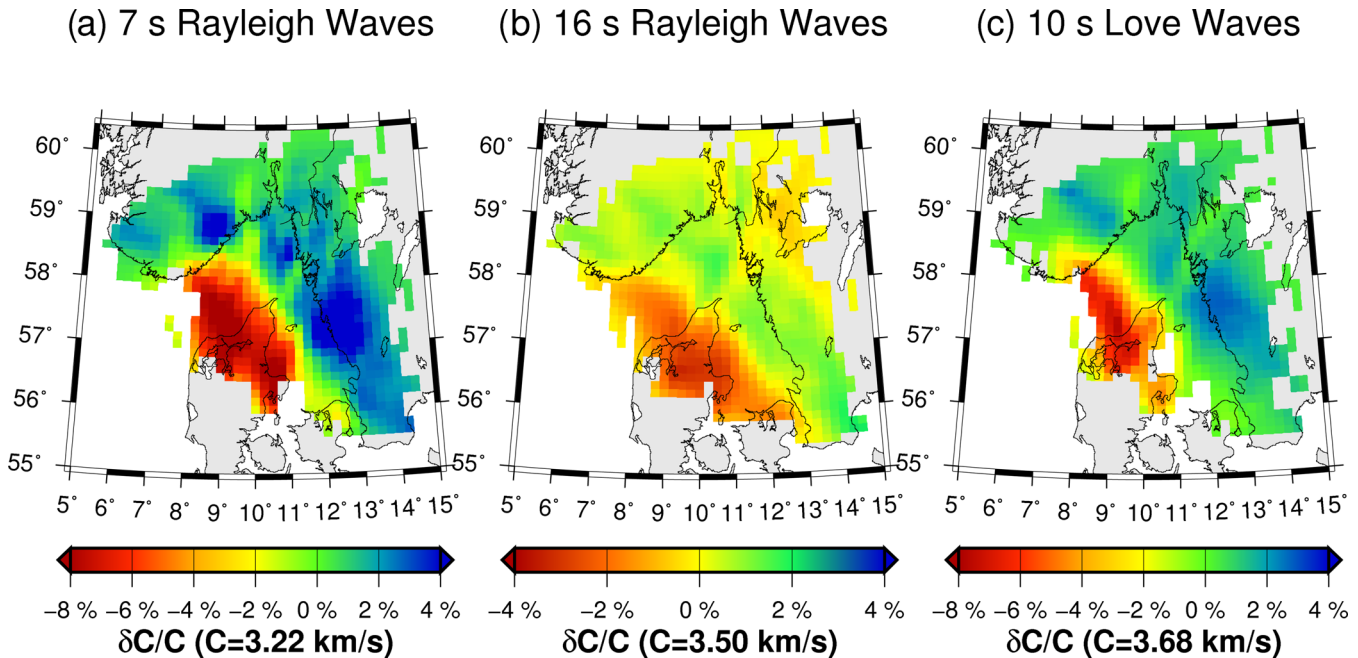


Figure 3. Rayleigh and Love wave phase-velocity maps at selected periods obtained by ambient seismic noise tomography. Grid nodes with resolution >40 km (see Fig. 4a) are excluded.

velocities for further inclusion in the tomography is restricted to measuring the signal-to-noise ratio (SNR) of each NCFs. The SNR must be higher than 12 for the broad-band signal and higher than 10 for the NCFs filtered at each target period used for the tomography. Furthermore, the phase-velocity measurements at each period must satisfy the requirement that the wavelength is shorter than one third of the interstation distance.

For station pairs with longer records, we also confirm the stability of phase-velocity measurements over time using independent NCF stacks over three months and stacks over all winter and summer months. No significant effect on the measured phase velocities are found. Uncertainties are lower than 0.05 km s^{-1} , and velocities of individual three-month stacks do not differ significantly compared to the result of the complete stack (Fig. A4). Hence, even station pairs with very short records are likely to produce reliable dispersion measurements.

In summary, the short stacking windows may introduce some potential uncertainty. However, the SNR has been shown to be a very robust selection criterion in many ambient noise studies. Furthermore, the reliability and stability of empirical Green's function estimates for station pairs with long records and for the network in the north of our study area (Köhler *et al.* 2011) is clearly given. It is safe to assume that directionality and temporal variations of the noise wavefield found in southern Norway are comparable to the situation in Denmark and southern Sweden. We are therefore confident that our selection criteria are sufficient to provide results without significant biases.

4.2 Phase-velocity maps

We invert for Rayleigh and Love wave phase-velocity maps using the tomographic inversion method of Barmin *et al.* (2001) using the same inversion parameters as in Köhler *et al.* (2011, 2012). A 0.2×0.2 deg grid and a starting model corresponding to the averaged observed velocity at each period is used. The following

regularization parameters are found to be most optimal (see, Barmin *et al.* 2001, for details): The regularization constant α is set to 400. It weights the spatial smoothing condition that depends on the correlation length σ which is set to 40 km. The term in the penalty function of the inversion that damps the norm of model depends on the path density at each period. Hence, more damping is used at periods longer than 20 s where the path density becomes poorer (see path number and path distribution maps in Figs A5 and A6). Fig. 3 shows a selection of phase-velocity maps after resampling on a 0.25×0.125 deg grid (more maps are shown in Figs 4c, A7 and A8).

Phase velocities as well as the variations of ± 3 per cent in Norway are in agreement with the results presented in Köhler *et al.* (2012). However, toward the south in the Skagerrak region and in Denmark, we observe strong negative velocity anomalies for Rayleigh and Love waves of about 8 per cent at short periods. In Sweden, positive velocity anomalies and average values comparable to those in Norway are observed.

Fig. 4(a) shows a resolution estimate of the tomography at 10 s based on the method of Barmin *et al.* (2001). It presents a summary of the information stored in the resolution matrix of the inversion. At each model node the resolution parameter represents the radius at the base of a cone fitted to the response of a delta anomaly. It can be interpreted as the minimum distance at which two delta shaped input anomalies can be resolved on the map. All inverted anomalies extend larger than about 35 km, which represents the worst obtained resolution at the edges of our model. Therefore, they can be considered as reliable (more resolution maps for all periods are given in Fig. A9).

Fig. 4(d) shows the result of a checkerboard test at 10 s. Despite of some smearing effects and amplitude damping, the inverted anomalies are generally well-defined. The location and size of synthetic anomalies is recovered sufficiently. Results at the edges of our model have to be interpreted with more caution. Smearing in NW–SE direction (dominant path direction) on the checkerboards occurs in areas with less path crossings, for example off-shore

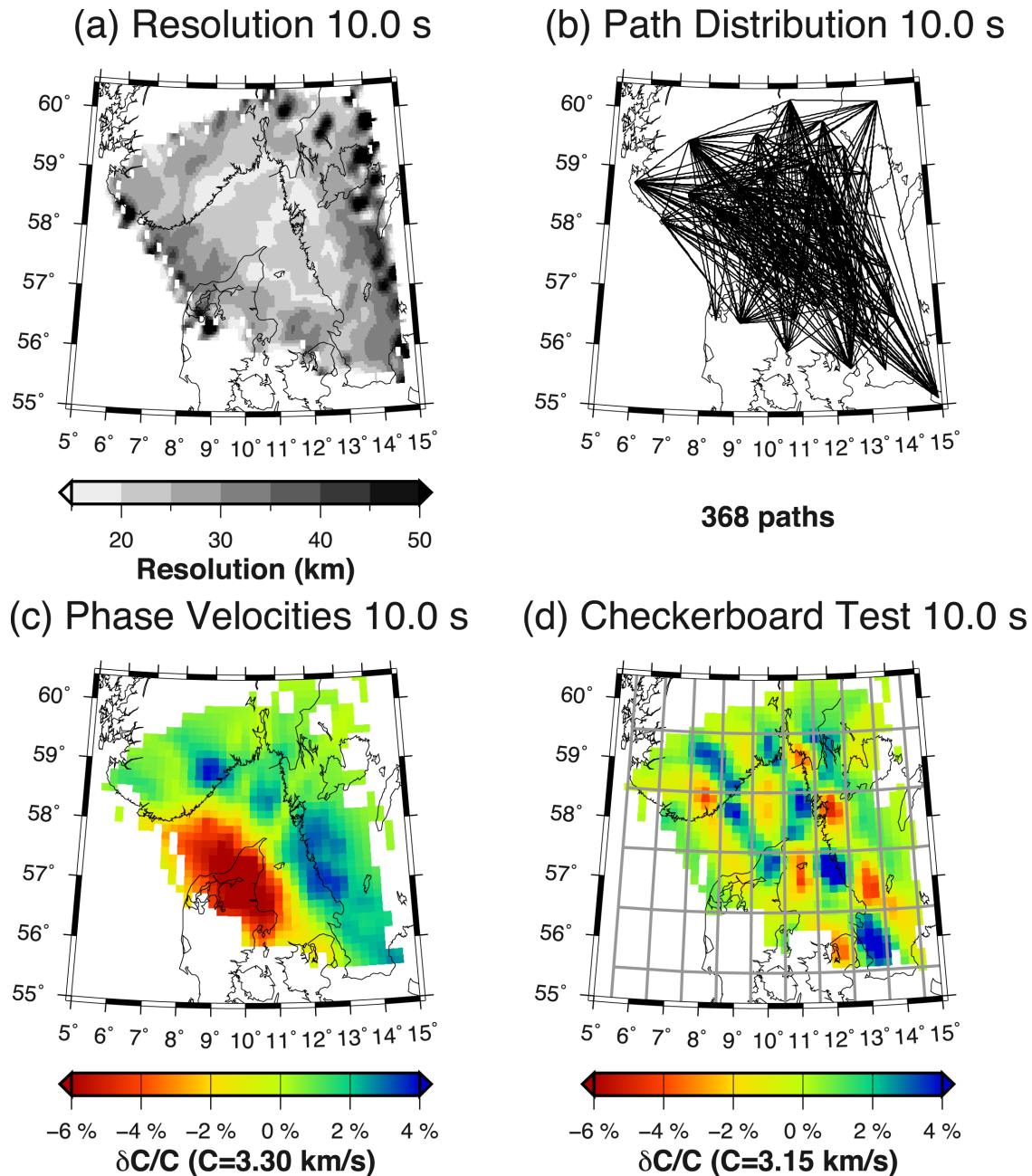


Figure 4. Resolution of the phase-velocity at 10 s period obtained using the method of Barmin *et al.* (2001) and the path coverage. Lower panels show the phase-velocity map together with the result of a checkerboard test. Synthetic velocity anomalies are -11.7 per cent and 5 per cent (alternating distribution in grey rectangular).

between Norway and Denmark as well as in Sweden to the east (more checkerboard maps for all periods are given in Fig. A10).

5 PHASE-VELOCITY CURVES FROM EARTHQUAKE DATA

The phase-velocity maps from ambient noise data are complemented at long periods by phase-velocity curves from earthquake data. The earthquake data set consists of 141 events (Fig. A11): 54 regional events with epicentral distances from 13 to 40° and magnitudes of at least 5.1 , and 87 teleseismic events with epicentral distances from 40 to 100° and magnitude of at least 6.0 , except for six events of magnitude 5.6 to 5.9 selected to improve the az-

imuthal coverage. In all cases, events have focal depths not larger than 100 km, ensuring dominant surface wave fundamental modes.

5.1 Methodology

Several techniques can be used to produce surface wave phase-velocity maps from earthquake data recorded at regional seismological networks (e.g. Friederich 1998; Forsyth & Li 2005; Prindle & Tanimoto 2006; Weidle 2012). Due to the modest dimension of the present network and the limited overlap in time of operation of the different stations, the data were not suitable for a tomographic analysis. Instead, we produced average phase-velocity curves for three different subregions using the beamforming analysis described in

Maupin (2011) and used in a study of the upper mantle just to the north of this study region.

The beamforming procedure produces for each event an average phase-velocity curve for the region covered by the subnetwork of stations. The phase-velocities are measured by forming, in the frequency domain, the cross-power spectra of the phase-shifted seismograms:

$$P(\omega, \vec{k}) = \sum_{i,j} a_i \exp(i\phi_i) a_j \exp(-i\phi_j) \exp(i\vec{k}(\vec{X}_i - \vec{X}_j)) \quad (1)$$

where a_i , ϕ_i , a_j and ϕ_j are spectral amplitudes and phases at stations i and j . $\vec{X}_i = (x_i, y_i)$ and $\vec{X}_j = (x_j, y_j)$ are coordinates of stations i and j in an event-dependent coordinate system that takes into account the curvature of the wavefront associated with the epicentral distance of each particular event. The phase-velocity is evaluated as:

$$c = \omega / k_{\max} \quad (2)$$

where ω is the circular frequency of the wave and k_{\max} the amplitude of the k -vector corresponding to the maximum value of the cross-spectra $P(\omega, \vec{k})$. We limit our measurements to cases where the cross-spectra are based on data that have passed some selection criteria at a minimum of six stations. The selection criteria are based on a comparison of the envelopes of the signals at the different stations in the whole network, as in Maupin (2011), with some further refinements to reject individual noisy data, as in Köhler *et al.* (2012). Examples of the distribution of phase velocities obtained for the three subnetworks at two selected frequencies can be found in Appendix (Fig. A12).

The phase-velocity curve retained for depth inversion in the next section is the median of all curves for a given subnetwork. This procedure increases greatly the stability and reliability of the phase-velocities curves compared to a tomographic analysis, but of course at the expense of lateral resolution. It is basically equivalent to a tomographic analysis using large lateral correlation lengths but with the advantage that *a priori* tectonic information is more easily taken into account with this procedure than with a more conventional tomographic analysis.

The configuration of the three subnetworks is shown in Fig. 1. The station selection has been made using tectonic information (Fig. 2) in order to group stations that are likely to belong to the same tectonic area, but also based on data availability at the different stations. Stations at the border between two subregions belong to two subnetworks and are therefore used twice. This ensures that there is no gap in the coverage of the area, and that the subnetworks are large enough for a stable determination of phase velocities. Subnetwork NOR covers the Norwegian part of the region west of the Oslo Graben. Subnetwork SWE covers southwestern Sweden. It includes two Norwegian stations at the Swedish border and the Danish island of Bornholm (station BSD), to the south of Sweden. The permanent station COP (Copenhagen) has also been included in this subnetwork due to its proximity to the Swedish coast. Subnetwork DEN covers the northeastern part of Denmark and the offshore areas of Skagerrak and Kattegat. This is achieved by including selected Norwegian and Swedish coastal stations in the subnetwork.

5.2 Phase-velocity dispersion curves

Rayleigh and Love wave phase-velocities curves are obtained for the three subnetworks in the period range 15 to a maximum of 100 s

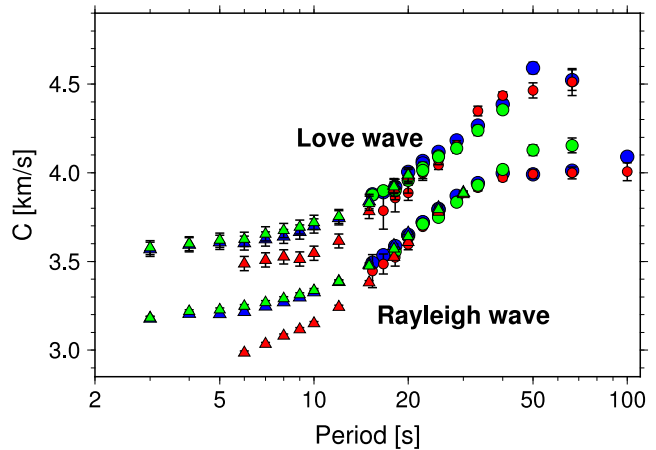


Figure 5. Rayleigh and Love wave phase-velocity curves at the three subnetworks DEN (red), NOR (blue) and SWE (green). Circles show the phase velocities measured with earthquake data, together with their error-bars. Triangles show the average phase velocities measured with ambient noise over the respective areas of the three subnetworks.

(Fig. 5). In the period range 15–25 s where we have overlap with ambient noise results, we note in general a good consistency with the curves obtained by averaging the velocities from ambient seismic noise over the relevant areas. The only significant discrepancy is for Love waves in the DEN subregion, where ambient noise data yield higher velocities than earthquake data. Velocities at periods from 15 to 22 s are calculated using regional events while velocities at periods from 22 s are calculated with the whole set of events. Phase velocities based on very few events or showing large scatter in the individual phase-velocity measurements have been removed from the final curves. This has affected mostly the Love waves at long periods. The total amount of data used to produce the phase-velocity curves can be found in Appendix (Figs A13 and A14).

The easternmost subnetwork SWE is quite elongated in the north–south direction, resulting in large spread for phase velocities measured from surface waves propagating perpendicularly to the subnetwork. In order to remove the influence of those outliers, we restricted the analysis to events in a broad backazimuth range aligned with the dominant direction of the subnetwork (140° – 220° and 320° – 40°). Although this reduces the scatter in phase velocities, it reduces also the number of measurements, leaving both median dispersion curve and error bars actually little affected by this selection. The only major consequence of backazimuth restriction is to increase the Rayleigh-wave phase velocities by 0.05 km s^{-1} at 50 and 70 s period and to decrease it by the same amount for Love waves at 30 s period. The Rayleigh wave dispersion curve for this subnetwork compares well with dispersion obtained by Cotte *et al.* (2002) from data registered further east in Sweden.

6 INVERSION OF LOCAL DISPERSION CURVES

We combine the Rayleigh and Love wave phase-velocity dispersion curves from ambient seismic noise tomography and earthquake phase-velocity curves in order to perform a joint inversion. The dispersion data comprises Rayleigh wave velocities from 3 to 30 s for ambient noise and 15 to 100 s for earthquake data. In the overlapping period band, ambient noise phase velocities and earthquake data are sampled at different periods, except at 20 and 25 s. We

Table 1. Ranges for model parameters in Inversion I. Note that layer 3 is parametrized by a range for thickness and not bottom depth. ' V_S in layer' refers to depth distribution of velocity within a layer, accomplished through five sub-layers. Density and V_P are uniform within each layer. Poisson ratio is limited between 0.2 and 0.5.

	Bottom depth	V_S	V_S in layer	V_P	Density
Layer 1	5–15 km	2.5–4.0 km s ⁻¹	Power law	2.5–7.0 km s ⁻¹	2.0–3.7 g ccm ⁻¹
Layer 2	15–40 km	3.0–4.0 km s ⁻¹	Linear increase	3.0–8.0 km s ⁻¹	2.2–3.7 g ccm ⁻¹
Layer 3	1–10 km (thickness)	3.5–4.5 km s ⁻¹	Linear increase	4.0–8.0 km s ⁻¹	2.2–3.7 g ccm ⁻¹
Layer 4	50–150 km	4.0–5.0 km s ⁻¹	Uniform	5.0–9.0 km s ⁻¹	2.5–4.0 g ccm ⁻¹
Half-space	–	4.2–5.0 km s ⁻¹	Uniform	5.0–9.0 km s ⁻¹	2.5–4.0 g ccm ⁻¹

average at those periods and use the remaining sampling periods independently. Fig. 5 shows that dispersion data obtained from ambient noise and earthquakes are consistent in the overlapping period band. The difference at 25 s is found to be smaller than 0.05 km s⁻¹ and of the same order as the measurement uncertainty of the individual methods. Phase-velocity measurements for Love waves are used between 3 and 20 s for noise and 15 and 66.7 s for earthquakes. Measurements at 20 s are averaged. Note that only the measurements at periods shorter than 30 or 20 s allow to invert for a true 3D velocity model at crustal depths. Data obtained at longer periods from earthquake data just allow to invert for an average velocity depth profile in each subnetwork region.

We follow the same inversion procedure as in Köhler *et al.* (2012). We invert for local velocity depth profiles on a 0.5×0.25 deg grid. In a first inversion step (Inversion I), we use the Neighbourhood Algorithm of Sambridge (1999), adapted and implemented to find isotropic, layered models fitting dispersion data (Wathelet *et al.* 2004; Wathelet 2008). Due to discrepancy between Rayleigh and Love waves, a second inversion run is conducted using a linearized inversion which takes into account radial anisotropy and adjusts the V_{SV} structure accordingly without changing interface depths (Inversion II). In order to find a good starting model for Inversion II, we only use Love waves up to 15 s together with the complete Rayleigh wave dispersion curve in Inversion I to avoid a bias on Moho depths due to anisotropy.

6.1 Inversion I

An empirical spherical correction is applied to the velocity measurements as in Köhler *et al.* (2012), since the implementation of the inversion has originally been developed to invert shallow models in a flat-earth setting. Any limitation of this procedure will be corrected in Inversion II, where sphericity is implemented fully.

The Neighbourhood Algorithm is a derivative-free, direct search algorithm which performs an iterative Monte Carlo sampling of the model space. The goal is to find an ensemble of models fitting the data, rather than a single optimal solution. The parametrization, constraints and *a priori* assumptions are summarized in Table 1. Three layers for the crust and one layer over half-space for the upper mantle are used. We invert for V_S , V_P , density and interface depths and finally select the 1000 best-fitting models at each location; see Köhler *et al.* (2012) for more details on used inversion parameters, misfit computation and model selection. The forward problem is solved with the method suggested by Dunkin (1965).

Fig. 6 shows the results of the inversion at three different locations in Denmark, Norway and Sweden. For the sites in Norway and Sweden, we observe a good fit between the measured and predicted dispersion curves. Fits with Love wave data are good at short periods for both locations as well as at long periods for the Swedish site. For the location in Denmark, however, we observe

that the predicted velocities are too low to fit the Love wave data. This Love–Rayleigh discrepancy shows that no isotropic model satisfying simultaneously the dispersions of both wave types could be found, and is usually considered as an indication for the presence of radial anisotropy. We also perform a second inversion run without using Love waves to evaluate a possible effect of anisotropy on inverted Moho depths. However, no significant difference is found.

6.2 Inversion II

Inversion II is a linear inversion that uses Rayleigh and Love waves to adjust the *S*-wave velocities found by Inversion I into the SV-wave velocity and the depth-dependent anisotropy parameter $\xi = (V_{SH}/V_{SV})^2$. The depth of the interfaces are kept fixed during inversion.

The starting model is computed by averaging the ensemble of best-fitting models from Inversion I for depths shallower than 140 km. From 140 km on, the velocities are linearly interpolated to the value of the ak135 model (Kennett *et al.* 1995) at 400 km depth. We conduct Inversion II following Tarantola & Valette (1982) for a simple linear inversion (see, Köhler *et al.* 2012, for details). Dispersion curves are forward computed using the implementation of Saito (1988). The model parameters V_{SV} and ξ we invert for are represented by a continuous function sampled at different depth points within each layer. The smoothness of the model variations with depth is controlled by an *a priori* correlation function that partly couples the variations of the parameter with depth through non-diagonal terms in the model *a priori* covariance matrix (see, Köhler *et al.* 2012, for details).

We choose the *a priori* standard deviation of the model parameters σ_m for V_{SV} to be 0.05 km s⁻¹ for Layer 1 and 0.1 km s⁻¹ for layers 2–4. For ξ we use $\sigma_m = 0.02$, and the correlation length increases linearly from 10 km at the surface to 50 km at 200 km depth. Velocity variations across Moho and crustal boundaries are decoupled. Finally, we evaluate the inverted depth distribution of V_{SV} and ξ at each location visually and increase the damping (i.e. decrease σ_m to 0.025 in layers 2 and 3) if necessary to avoid unrealistic oscillation of model parameters in the crust at some locations (see Fig. 10). Taking into account radial anisotropy reduces the misfit considerably (Fig. 7). The inverted models now explain both Rayleigh and Love wave velocities.

7 RESULTS

7.1 3-D shear wave structure

Representative examples of velocity versus depths for the three different geographic and tectonic areas: northern Denmark, southern Norway and the southwestern part of Sweden, are shown in Fig. 7. Figs 8(a)–(f) show the results of the inversion in terms of maps

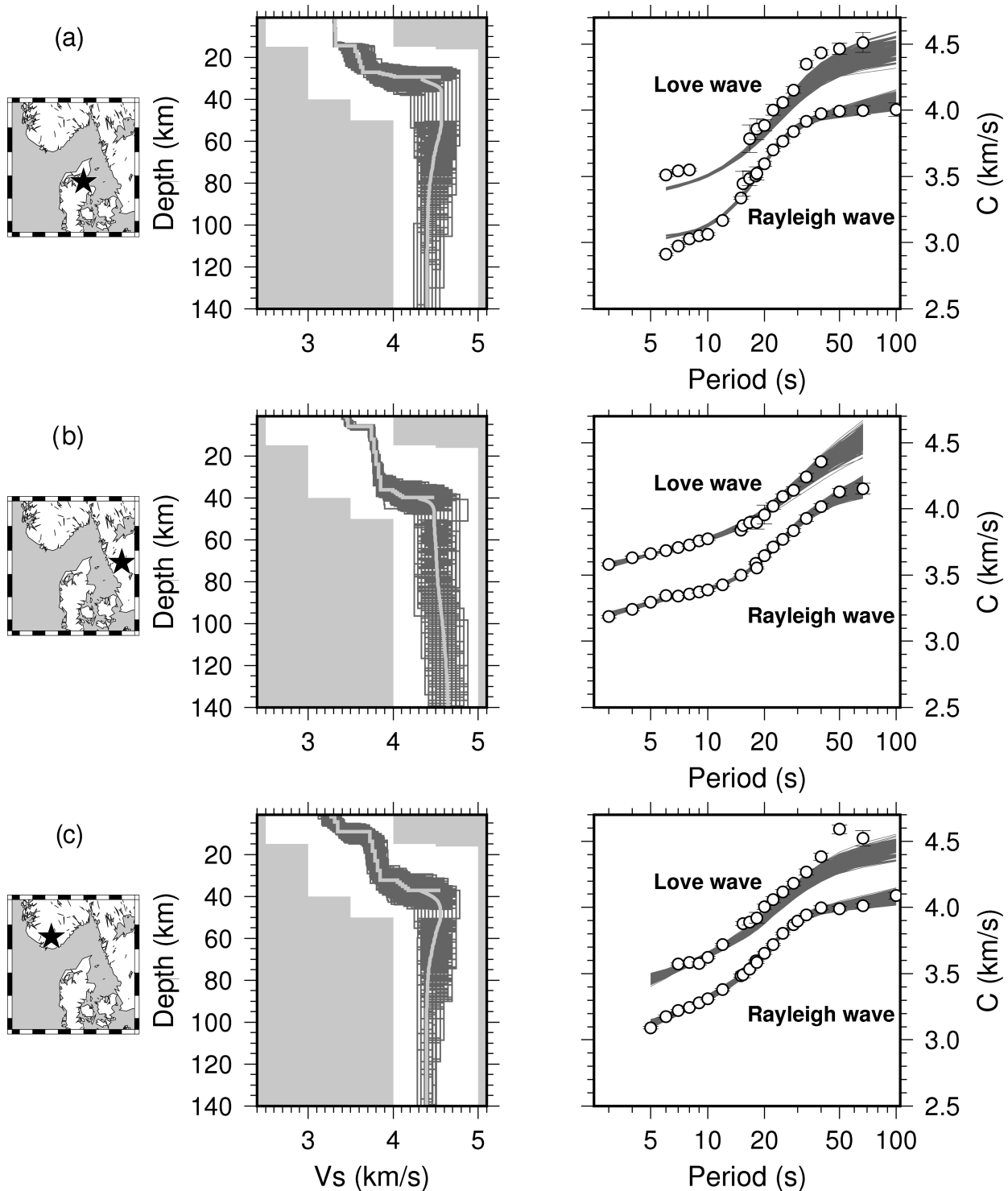


Figure 6. Representative examples of inverted velocity models, Inversion I: star in leftmost panel indicates location. Dark grey V_S profiles are ensemble of best-fitting models. Light grey profile is corresponding averaged model. Rightmost panels: symbols show measured phase velocities, grey lines dispersion curves of best-fitting models. Note the bad fit to the phase velocities of Love waves, showing that anisotropy is required.

of average SV-wave velocities in different selected depth ranges. No lateral smoothing is done at this stage, that is, the velocities for each, independently inverted 1-D profile are shown. Vertical cross-sections with slight smoothing are shown in Fig. 9. Note that small-scale lateral variations are not resolved at mantle depths where we invert averaged earthquake dispersion data for each of the three subnetworks.

7.1.1 Crust

At shallow depths (4–8 km), lateral velocity variations correlate well with known near-surface geology. The shear-wave structure is clearly dominated by the contrast between the low velocities in the Danish Basin, which extends into the Skagerrak area (*cf.* Fig. 2), and higher velocities in the crystalline crust of Norway

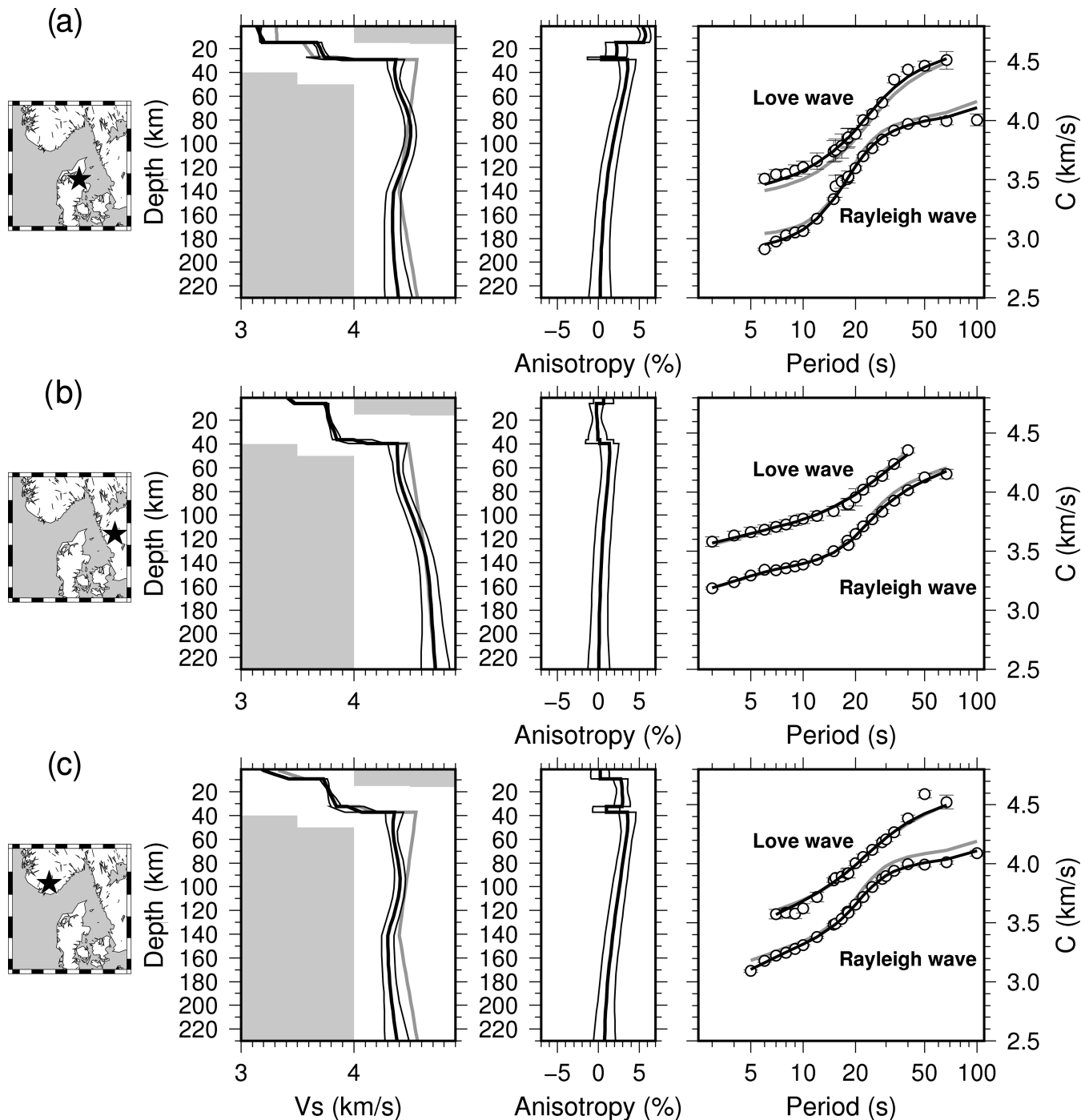


Figure 7. Representative examples of inverted velocity models, Inversion II: star in leftmost panel indicates location. Light grey profile is initial model obtained from Inversion I. Black profile for V_S (V_{SV}) and radial anisotropy shows final model. Thin black lines indicate *posterior* model standard deviation. Rightmost panels: symbols show measured phase velocities, grey line dispersion curve of initial model, and black line fit of final model.

and Sweden. The total velocity contrast here is about 0.8 km s^{-1} , more than twice as large as found further north in southern Norway (Köhler *et al.* 2012). A high horizontal contrast from the Skagerrak–Kattegat Platform, with a thin sedimentary cover, into the deeper parts of the Danish Basin is clearly revealed. This is consistent with the results of refraction seismic lines crossing the areas of northern and central Jutland (Eugeno-S Working Group 1988; Knudsen *et al.* 1991; Sandrin & Thybo 2008). Sedimentary rocks with P -wave velocity between 1.9 and 5.5 km s^{-1} are observed to depths between 1.5 km , to the northeast, and 10 km in the deepest part of the basin,

where Fig. 8(a) shows low S -wave velocity. Low velocities very close to the Norwegian coast are probably a result of smearing from the sedimentary areas further south, due to the configuration of the seismological stations.

The upper crust, at the depth interval of 10 – 14 km , shows large lateral velocity variations ($c. 3.2$ – 3.8 km s^{-1}), again with the lowest velocities in the Danish Basin, indicating reduced velocity also in the shallow crystalline/metamorphic basement below the sediments. Some velocity variations are observed also in the middle/lower crust (16 – 24 km) with some local very low values in the northeastern

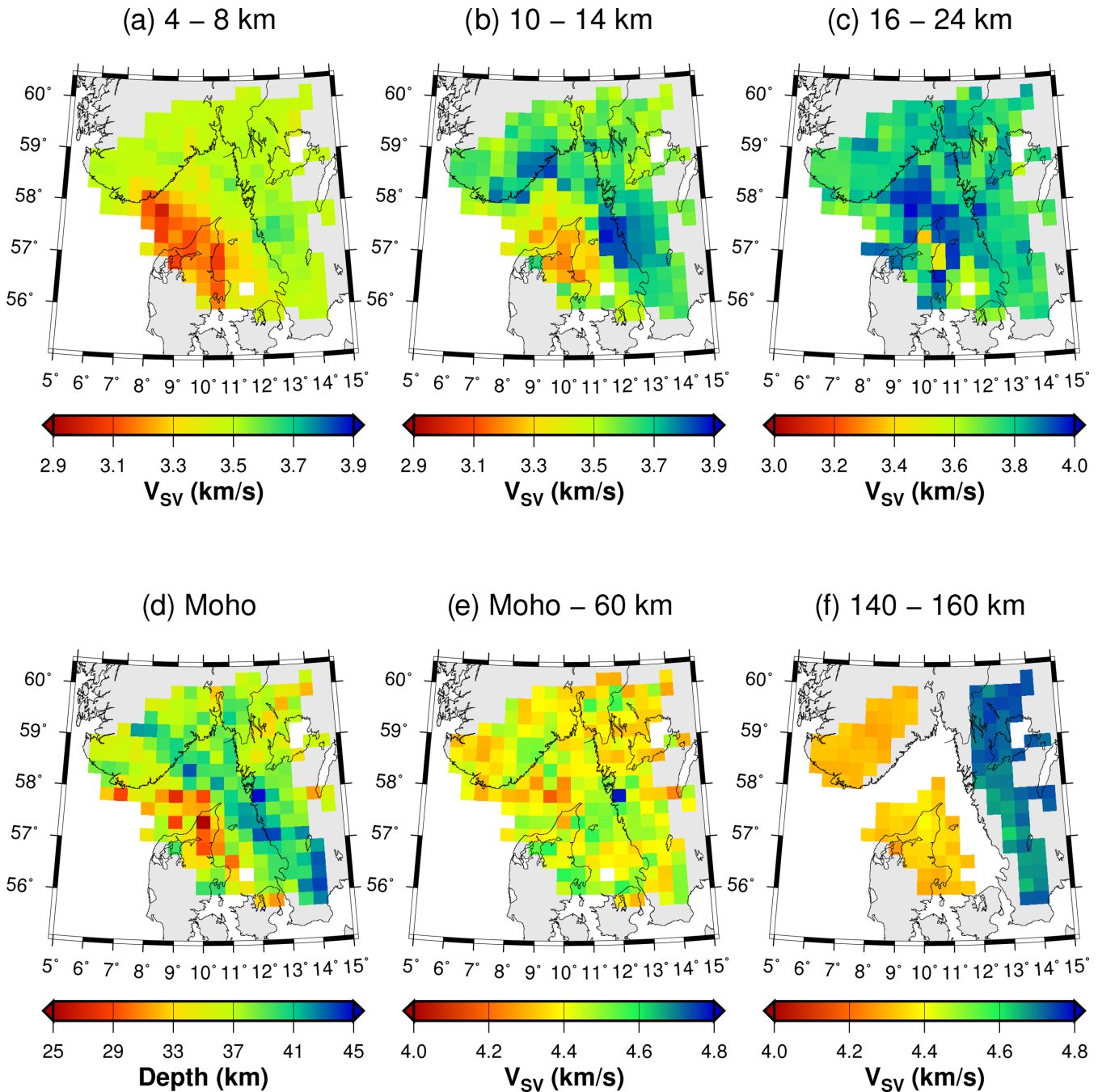


Figure 8. Final inverted V_{SV} model. (a)–(f) Velocities averaged in different depth ranges are shown. At mantle depths, the model is shown in three disconnected areas to emphasize that only average models in three subregions are available. See also Fig. 2 for outline of main geological units.

part of Denmark (see discussion on trade-off with Moho in the next section), but generally S -wave velocities are around 3.8 km s^{-1} . This level is consistent with S -refraction results in southern Norway (Stratford & Thybo 2011) as well as P -wave velocities of about 6.5 – 6.6 km s^{-1} obtained in several refraction experiments in the study area (e.g. Eugeno-S Working Group 1988; Sandrin & Thybo 2008; Stratford *et al.* 2009).

Positive crustal velocity anomalies (3.8 – 4.0 km s^{-1}) are observed in the coastal areas of southwestern Sweden (around 57 – 58 N, Figs 8b and c) and extending to the northwest into the Kattegat and Skagerrak. These velocity anomalies seem to correlate with positive gravity anomalies (up to 25 – 30 mgal,

e.g. Eugeno-S Working Group 1988, fig. 9) likely caused by dense mafic intrusions of Late Carboniferous–Early Permian age, and thus of the same age as the main volcanism in the Oslo Graben area (see modeling results in Thybo (2001) and discussion below).

The *posteriori* standard deviation of V_{SV} is shown in Fig. 10(a) averaged over the depth range from 4 to 20 km. Note that the uncertainty is lower at those locations where we had to use a stronger damping in order to avoid oscillation of model parameters (see Fig. 10d). The model uncertainty is not larger than about 0.04 km s^{-1} in the crust which supports the reliability of the discussed velocity anomalies.

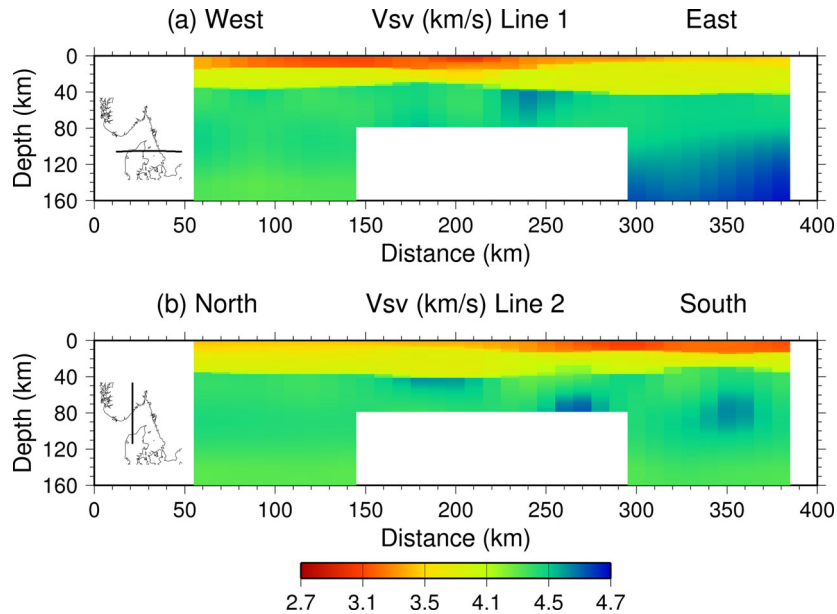


Figure 9. Cross-sections through the final model along lines shown in the inset. A lateral smoothing of the original model is applied by averaging in 1×0.5 deg cells and resampling at 0.25 deg. At mantle depths, only average models in three subregions are available. Transitional areas are therefore shown in white to emphasize that those depths are not resolved.

7.1.2 Moho depth and its trade-off with adjacent layers

The interface between layers 3 and 4 is interpreted as representing the boundary between crust and mantle (the Moho, Fig. 8d). Although with some local scatter in depth, likely to reflect mainly resolution uncertainty, a clear trend is observed with Moho depth increasing from about 30 km in northern Denmark and the western part of the Skagerrak to about 40 km along the Swedish coast. This is consistent with results of several refraction lines (Eugenio-S Working Group 1988) and receiver function analysis along the TOR profile further to the south (Alinaghi *et al.* 2003). Considering that this trend does not correspond to one of the *a priori* boundaries used in the analysis of the earthquake data, this shows that Moho depth is constrained by the ambient noise data and is not, or at least not much, affected by the limitations of the earthquake data set. The locations and sharpness of the contrasts can therefore be interpreted.

This increase in crustal thickness of about 10 km occurs over a short distance of less than 100 km. We note that the thin crust correlates with the areas of low *S*-velocity in the upper crust that reflect the thick sedimentary sequences in the Danish Basin. The area with thin crust in northern Denmark shows low velocities both in the lower crust and in the upper mantle, and we have to analyse if these features in our models are not merely the result of trade-offs between these parameters.

The depth range 16–24 km is significantly above Moho in Sweden and in southern Norway, but closer to Moho in Denmark. It can be clearly seen from the set of acceptable models in Fig. 6 that the velocities at around 20 km depth are much better constrained in the example model from Sweden, and also partly from Norway, than in the example model from Denmark. It is therefore likely that the larger variability in lower crustal velocities seen in Denmark in Fig. 8(c) is a result of trade-off with the rather shallow Moho in this area. The more stable values of 3.8 km s^{-1} seen in southern Norway and Sweden are much better resolved.

Köhler *et al.* (2012) explored the resolution potential of our inversion procedure with respect to Moho depth versus upper-mantle

velocity for a data set very similar to this one. By forcing Moho depth upward by 4 km from its inverted values results in sub-Moho velocities decreasing by 0.2 km s^{-1} , but in no significant change at 100 km depth. Considering possible trade-off between Moho depth and sub-Moho velocity, we conclude that the small-scale lateral variations of about 0.2 km s^{-1} present in the map for Moho-60 km depth (Fig. 8d) cannot be interpreted with confidence, and we can only infer that velocity just below Moho in our study area is about 4.5 km s^{-1} .

Due to the trade-off between Moho depth and velocity, the accepted models in Inversion I show larger spread at Moho and sub-Moho depths (Fig. 6). At larger depth, trade-off with Moho is less significant, leading to a smaller uncertainty, apparent as a reduced spread in the models in Inversion I (Fig. 6). This is particularly true in Norway and Denmark where Rayleigh and Love waves are measured at the largest periods. However, the spread of models stays larger in Sweden since Rayleigh wave velocity at 100 s and Love wave velocity at 66 s are missing to better resolve the corresponding depth range.

Standard errors for Moho depths of about 500 m on average (Fig. 10c), obtained by averaging the ensemble of best-fitting models of Inversion I at each location, seems to be underestimated. Given model parameters trade-offs as discussed above and spread between adjacent grid cells, a Moho uncertainty of about 3 km is more realistic.

7.1.3 Upper mantle

At deeper upper-mantle levels, velocities are mostly constrained by the earthquake data and the location of the lateral velocity gradients in the mantle merely reflects our choice of subnetwork geography. The velocities have therefore been plotted in three distinct geographic areas in the lower layer (Fig. 8f) to emphasize that the detailed locations of the boundaries and gradients are not constrained. The high-velocity anomalies in the southern part of Line 2 (Fig. 9b)

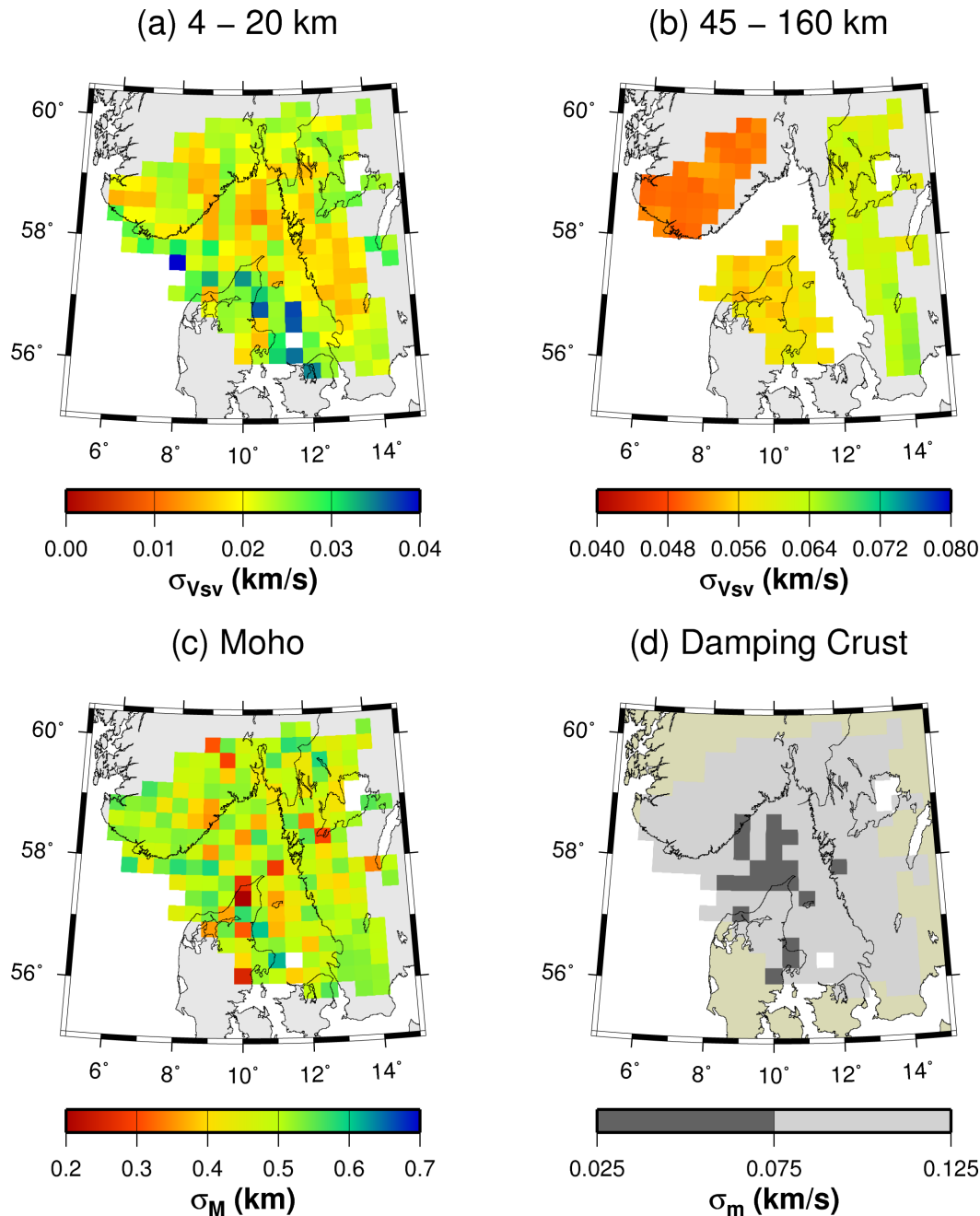


Figure 10. (a)–(c) Uncertainty of inverted models. Standard deviation of V_{SV} is averaged for two depth ranges. Standard deviation of Moho depth is obtained from averaging the ensemble of best-fitting models after Inversion I. (d) Averaged *a priori* standard deviation (damping) in crustal layers. It is set to $\sigma_m = 0.05$ in layer 1 and $\sigma_m = 0.1$ in layers 2 and 3. At some locations damping is manually increased in layer 2 or 3 by setting σ_m to 0.025.

in Denmark at a depth level of 80 km may be related to the Moho trade-off (low sub-Moho velocities) as discussed above (Fig. 7a).

Below 100 km depth, the contrasts are well resolved and significant. The *posteriori* standard deviation of V_{SV} is not larger than 0.065 km s^{-1} (Fig. 10b). Maximum contrasts of about $0.30\text{--}0.40 \text{ km s}^{-1}$ are observed in the 140–180 km depth range (Figs 8f and 12) with low S -velocity in southern Norway (c. 4.3 km s^{-1}) and northern Denmark ($4.3\text{--}4.4 \text{ km s}^{-1}$) and significantly higher velocities, $4.6\text{--}4.8 \text{ km s}^{-1}$, in southern Sweden. At that depth level both the Norwegian and Danish areas show a marked low-velocity zone, which seems to start at a depth of about 100 km, in marked contrast to southern Sweden

with a positive velocity gradient down to the bottom of our model (Fig. 12).

Since the longest periods are missed for velocity measurements in Sweden (Fig. 5), we performed several tests to check the robustness of the velocity difference between Sweden and the remaining parts at depths below 100 km. Using the same starting model in the mantle for all three regions, the results always show higher velocities in Sweden by at least 0.2 km s^{-1} , even when the variance of the *a priori* model is set to 0.1 km s^{-1} only.

Our results are consistent with and add new information to previous P -wave (Medhus *et al.* 2012; Kolstrup *et al.* 2015) and S -wave (Wawerzinek *et al.* 2013; Kolstrup *et al.* 2015) traveltimes

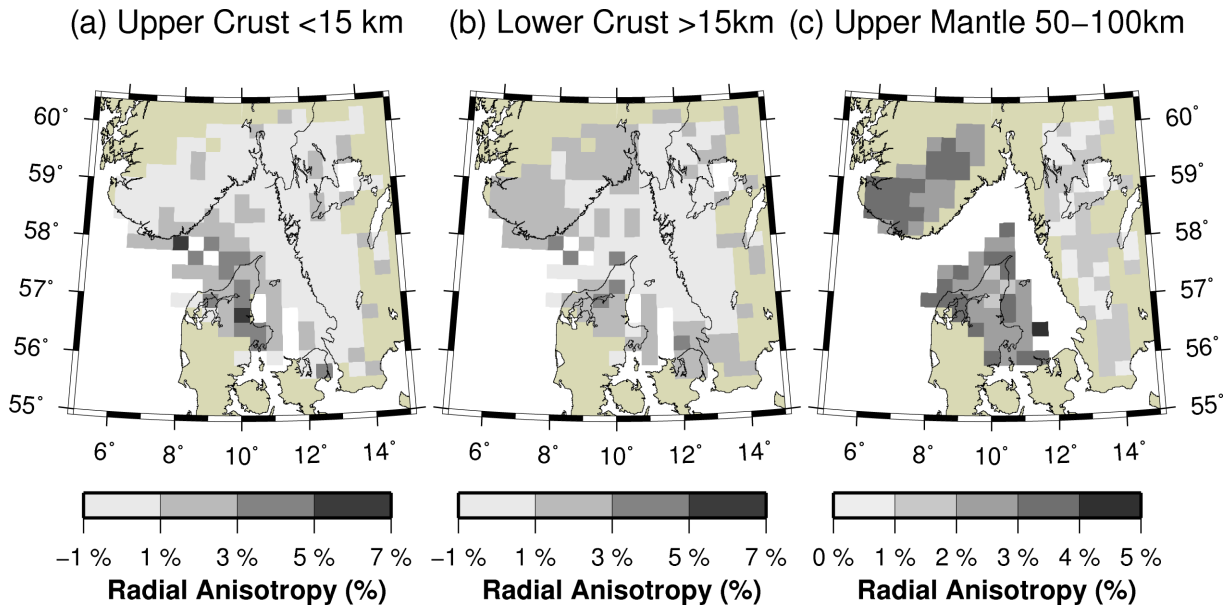


Figure 11. Difference between V_{SH} and V_{SV} (radial anisotropy, positive for $V_{SH} > V_{SV}$) in percent with respect to mean of both velocities, averaged for different depth ranges. Grid locations where Love wave data are not available at short periods are omitted (white gaps).

tomography results as well as results of surface wave analysis (Pedersen *et al.* 1994; Cotte *et al.* 2002; Maupin 2011) also showing marked differences in upper-mantle velocity between southern Sweden, with high velocity to great depth, and Denmark and southern Norway with reduced velocity. Recent high-resolution full-waveform regional S -wave tomography by Rickers *et al.* (2013), covering the North Atlantic region, also shows a clear low-velocity layer in the upper mantle below southwestern Scandinavia, and they suggest a sub-lithospheric connection from the North Atlantic areas.

7.2 Radial anisotropy

The inverted ξ value is transformed to relative difference between SV- and SH-wave velocities and plotted in Fig. 11 over different depth ranges. We infer positive anisotropy ($V_{SH} > V_{SV}$) in some distinct areas, both in the crust and in the mantle.

In the crust, the strongest anisotropy, with about 3 per cent on average, occurs in the upper crust in the Danish Basin, in the area characterized by low V_{SV} and a thick sedimentary basin (Fig. 11a). As strong layering will appear at the periods used here as transverse isotropy, it is likely that at least part of the anisotropy observed here is directly related to the layering in the sedimentary basin. At lower crustal depths, radial anisotropy decreases in amplitude to values between 1 and 3 per cent, but arises in a larger area extending into southern Norway and the southeastern part of the study area. Compared to the amplitude of middle to lower crustal anisotropy of up to 5 per cent found using the Love–Rayleigh discrepancy in ambient noise data in other regions (Moschetti *et al.* 2010a,b; Cheng *et al.* 2013; Dalton & Gaherty 2013), the amplitude of the anisotropy found here is not excessive (Fig. 11b). It does not correlate clearly with the velocity in the lower crust or Moho depth but rather with the upper-mantle velocities at 150 km depth (Fig. 8f).

In the uppermost mantle below the Moho, positive anisotropy between 2 and 4 per cent is required to explain Rayleigh and Love wave observations at periods larger than 30 s in southern Norway and northeastern Denmark (see Figs 6b and 11c). This is slightly

stronger than the anisotropy of 1.5–2 per cent found just to the north (Köhler *et al.* 2012). In contrast, no significant anisotropy is required in the Swedish subregion. The decrease of anisotropy with depth is related to the lack of resolution at depth and should not be interpreted.

8 DISCUSSION

A surface wave tomography study as the present, which combines ambient noise and earthquake data, yields S -velocity information from near-surface level to significant depth into the upper mantle. By applying this method in our study region of southwestern Scandinavia, we are able to study relationships between near-surface geology and structures at depth in a region with marked tectonic and morphologic contrasts. Compared with previous controlled source studies, providing seismic velocity information along profiles, we have here 3-D crustal and uppermost mantle velocity information. The regional body-wave teleseismic tomography studies by Medhus *et al.* (2012), Wawerzinek *et al.* (2013), Hejrani *et al.* (2015) and Kolstrup *et al.* (2015), based on very good seismological station coverage, also provide detailed areal coverage, but not from the crust (due to lack of resolution) nor from the shallow uppermost mantle (due to upward smearing). Therefore, this study provides significant new seismic velocity and structural information.

The main tectonic boundary of our study area, which is marked by the transition from old Baltic Shield in southern Sweden to younger deep sedimentary basins in most of the Danish area (along and close to the STZ, Fig. 2), is clearly reflected in the seismic velocity distribution at almost all depth levels (Fig. 8). The tectonic transition from southern Norway across the Skagerrak to the Danish area also represents a boundary between exposed Precambrian units and deep basins, and, in addition, includes the transition from the southern Scandes Mountains to the lowlands to the south. This structural transition is marked by differences in crustal velocity distribution, in particular in the upper part of the crust, and by differences in crustal thickness. In contrast to the tectonic transition between Denmark and southern Sweden, the transition between

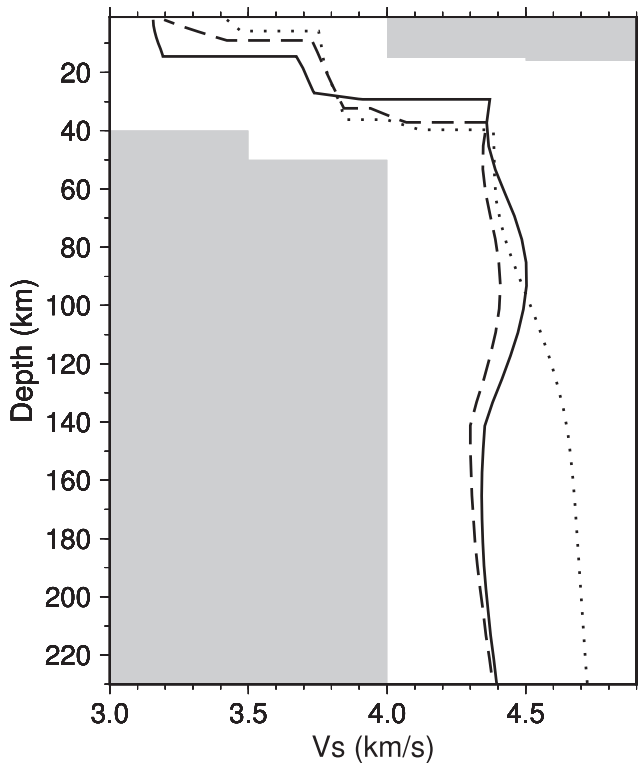


Figure 12. Comparison of inverted V_{SV} profiles of three sub-regions (cf. Fig. 1): southern Norway (dashed line), northeastern Denmark (solid line) and southwestern Sweden (dotted line).

Denmark and southern Norway is not marked by clear differences in the velocity and anisotropy of the upper mantle (Figs 8f, 9, 12 and 11).

The Danish Basin and its extension into the Skagerrak are clearly revealed by low velocities in the 4–8 km depth interval (Fig. 8a). In general, the basin is unlikely to have sedimentary thicknesses much beyond a maximum of about 10 km as mapped by control source seismology (Knudsen *et al.* 1991; Sandrin & Thybo 2008). Reduced seismic velocity at the depth of 10–14 km (Fig. 8b) may in part reflect deeper sediments locally, and also to some extent be caused by the existence of higher temperatures below thick sediments. Geothermal gradients in the basin are 25–30 °C km⁻¹, in contrast to typically significantly lower values, around and slightly above 15 °C km⁻¹, in the adjacent Precambrian uppermost crust (Balling 1992, 1995; Slagstad *et al.* 2009). This results in temperatures being 100–150 °C higher at upper crustal levels below the deeper parts of the basin.

Characteristic crustal thinning beneath the basin is clearly seen by a shallow Moho (Fig. 8d) below areas of thick sediments resulting in a significantly thinned crystalline crust. A thinned crust is a result of basin formation in which lithospheric stretching is found to form the dominant mechanism (Frederiksen *et al.* 2001). Basin initiation with lithospheric extension and crustal thinning was stimulated by significant Late Carboniferous–Permian tectonic and volcanic activity in the North Sea region. The present-day boundary between upper mantle of contrasting seismic velocity (here represented by the depth interval of 140–160 km, Fig. 8f) is found along or very close to the eastern boundary of a branch of significant tectonic and volcanic activity in the Kattegat, Skagerrak and Oslo Graben areas as outlined in Heeremans & Faleide (2004). This upper-mantle velocity boundary, accurately delineated at depth

by the body-wave traveltimes tomography (Medhus *et al.* 2012; Wawerzinek *et al.* 2013; Hejrani *et al.* 2015; Kolstrup *et al.* 2015), is found running along the southwest coast of Sweden, continuing north into southern Norway in the Oslo Graben area, exactly between our areas of different upper-mantle velocity. The body-wave tomography results show the continuations of this velocity boundary further north across southern Norway as well as the continuation of upper-mantle low velocities to the south in the Danish area and into northern Germany. This study constrains the upper boundary of the low-velocity zone below the Danish area and southern Norway at a depth of about 100 km (Figs 7 and 12). This depth is not resolved in the body-wave models, due to significant upward smearing (cf. checkerboard and block-model tests in Medhus *et al.* 2012).

Temperature differences are likely to play an important role in explaining deep velocity differences between shield areas of southern Sweden, with lower heat flow (about 55–60 mW m⁻², outside areas enriched in heat producing elements) than the Danish Basin (about 70 mW m⁻²). Thermal modeling (Balling 1995) shows depth to ‘base thermal lithosphere’ (c. 1300 °C) at about 100 km depth below the Danish Basin. Combined with present results, this consistently indicates lithosphere of about 100 km thickness below the Danish Basin and the existence of a clear low-velocity asthenosphere below the lithosphere.

No low-velocity zone is seen below southern Sweden with high velocities continuing to the bottom of our model at about 200 km depth (Fig. 12). This is in accordance with body-wave tomography models showing high velocities to depths of 300 km and more. Upper-mantle velocity contrasts between southern Sweden and the Danish areas, here clearly demonstrated for the depth interval of 100–200 km, is thus interpreted as representing differences between thick shield lithosphere and relatively shallow basin asthenosphere. This interpretation is in accordance with seismological (Gregersen *et al.* 2010), magnetotelluric (Smirnov & Pedersen 2009), as well as geodynamic convective models by Hieronymus *et al.* (2007) from the area of the seismological TOR profile crossing the STZ in the southeastern part of our study area.

The upper-mantle velocity contrasts between southern Norway and southern Sweden, and the associated similarity between southern Norway and the Danish area (Figs 8f, 9 and 12), is less easily understood. The existence of low upper-mantle velocity below southern Norway cannot be questioned. As mentioned above, our results are fully consistent with independent body-wave traveltimes tomography models, for P waves (Medhus *et al.* 2012) and S waves (Wawerzinek *et al.* 2013) as well as surface wave models by Maupin (2011) and Köhler *et al.* (2012), which include data from more stations across southern Norway.

Variations of seismic velocity in a peridotitic upper mantle are caused by temperature and/or compositional differences with temperatures generally being the more important (cf. Lee 2003; Hieronymus & Goes 2010; Schutt & Leshner 2010). Compositional differences seem to account for velocity variations of no more than up to about 1 per cent. Structural differences, such as anisotropy, may play a part as well.

Recent traveltimes tomographic models by Hejrani *et al.* (2015) and Kolstrup *et al.* (2015), with information on both P -wave and S -wave velocity and their ratio across this study area, suggest that compositional differences may play a part along the whole of the main upper-mantle velocity boundary. The ratio between P -wave and S -wave velocity seems to be a fairly robust indicator of compositional differences (Lee 2003; Schutt & Leshner 2010). Differences in this ratio of 2 per cent are observed across the velocity boundary, with generally low values in shield areas to the east and higher

values in basin areas to the southwest and in most of southern Norway. This observation is taken to support the interpretation of thick depleted relatively cold shield lithosphere in southern Sweden contrasting with more fertile, warm mantle asthenosphere beneath the Danish Basin and, perhaps, beneath large areas of southern Norway as well. Compositional differences across the upper-mantle boundary between southern Norway and Sweden is also present in the integrated geophysical-petrological models presented by Gradmann *et al.* (2013), who test different lithospheric mantle thicknesses and bulk compositions against observed seismic velocities, gravity anomalies and topography.

The S -velocity model of Rickers *et al.* (2013) for the North Atlantic region, with adjacent continental areas of northwestern Europe and Greenland, has a better resolution than other similar regional models and reaches great depths into the mantle. In addition to strong negative velocity perturbations in the vicinity of the hot spots along the Mid-Atlantic Ridge, this model shows apparently well-resolved ‘sub-lithospheric low-velocity fingers’, with a significant velocity reduction (more than 2 per cent) at depths of around 120–180 km, which extend far from the ridge. One finger reaches the southwestern part of Norway and further into the Danish area, but not into the shield areas of southern Sweden. According to Rickers *et al.* (2013), this suggests a flow of low-velocity hot spot material not only along-ridge, but also in directions away from the ridge and over very long distances. Such observation seems to be among the most important for our understanding of similarities and differences in upper-mantle velocity structure beneath our study area.

We observe anisotropy of about 2–3 per cent (with $V_{SH} > V_{SV}$) in some parts of the crust and of the mantle. This anisotropy is an interpretation in terms of vertical transversely isotropic structure of the fact that the Love wave phase velocities are too high compared to the Rayleigh wave phase velocities and do not pretend to characterize the whole anisotropy of the model, in particular its azimuthal anisotropy. The presence of anisotropy in the mantle has been recognized for several decades, but the deeper crust has up to recently been considered as rather isotropic. Several surface wave studies based mostly on ambient noise have recently challenged this view and proposed that the deeper crust may be more anisotropic than initially assumed. Although extended lower crustal anisotropy seemed at first to characterize areas of strong and recent crustal deformation (Moschetti *et al.* 2010a,b; Cheng *et al.* 2013), Dalton & Gaherty (2013) have also inferred strong mid-crustal anisotropy of 5 per cent in the northwestern Canada craton. Weiss *et al.* (1999) and Erdman *et al.* (2013) argue that rock texture, in particular in mica-rich environment, can account for lower crustal anisotropies of up to 5–7 per cent. Horizontal foliation in the lower crust can thus easily explain the amount of anisotropy found here. In the uppermost part of the crust, cracks are often considered as a major factor for anisotropy, but for vertically aligned fluid-filled cracks, the azimuthal-average SV and SH velocities are equal and no Love–Rayleigh discrepancy will be observed. The alignment of minerals in sedimentary basins is on the other hand a factor that does produce radial anisotropy of the amplitude found here in the Danish basin, in particular in the presence of phyllosilicates (Valcke *et al.* 2006).

In contrast to southwestern Sweden, we observe upper-mantle anisotropy of 2–4 per cent in southern Norway and northeastern Denmark in the depth range 50–100 km. As anisotropy loses resolution with depth faster than the SV velocity due to the smaller penetration depth and lack of long-period data in the Love waves, we cannot infer if radial anisotropy is also present at the depth of the low velocities, below 100 km. Although it is observed at shal-

lower depths, the radial anisotropy is located in the two subregions showing mantle low velocity, suggesting they have a common origin in mantle dynamic processes. Horizontal alignment of olivine in the mantle produces primarily azimuthal anisotropy which cannot be detected with the present data. Seen by surface wave velocities averaged in different azimuths, as in the present case, it does however appear as radial anisotropy with $V_{SH} > V_{SV}$ (Maupin 1985; Maupin & Park 2007). The amplitude of 3 per cent observed here is compatible with a percentage of oriented olivine crystals close to 50 per cent and with the amplitude of radial anisotropy observed in other similar regional studies (see Maupin & Park 2007, for a review). The collocation of the anisotropy and the low velocities does therefore strengthen arguments for their dynamic origin and the possible relation to the Mid-Atlantic Ridge (Rickers *et al.* 2013). One could also argue that it suggests a dynamic influence of the asthenospheric flow on the lithosphere above.

9 CONCLUSIONS

We have constructed a model of S -wave velocity and anisotropy in the crust and upper mantle across the northern part of the Tornquist zone (the Sorgenfrei–Tornquist zone). This model is based on the analysis of ambient noise and teleseismic surface waves and bridges in depth the models of the deeper mantle that have been obtained from body-wave tomographies and the more local crustal studies. In the upper crust, we map the thick sedimentary Danish Basin both with low S -wave velocities and velocity anisotropy ($V_{SH} > V_{SV}$). Moho depth and trends of variations are in agreement with previous studies showing marked crustal thinning beneath the Danish Basin, but trade-off with lower-crust and uppermost-mantle velocities prevents a very good resolution of this boundary using surface waves only. Upper-mantle velocities are found to be lower in Denmark and southern Norway than in southern Sweden by 0.30–0.40 km s⁻¹ (6–8 per cent) at the depth levels of 140–200 km. Sweden has high velocities and thick lithosphere characteristic of shields. In contrast, Denmark and southern Norway have well-defined low-velocity zones (interpreted as asthenosphere) starting at a depth of about 100 km. Furthermore, significant radial anisotropy of 2–4 per cent is observed in those regions. Thus, despite tectonic units of our study area all have old Precambrian Baltica crustal basement of quite similar origin, we observe very different present-day lithospheric and sub-lithospheric structures. We interpret these structural differences as due to a different tectonic and dynamic history with attenuation and reworking of cratonic lithosphere (Denmark and southern Norway) along the southwestern boundary of thick Baltica lithosphere in southern Sweden. Our studies confirm the importance of the Northern Tornquist Zone, as a very deep structural boundary. Recent high-resolution full-waveform tomography models indicate, that the sub-lithospheric low-velocity zones in southern Norway, and perhaps in Denmark as well, at least in part, may be explained in terms of a connection to hot upper-mantle plume systems in the North Atlantic.

ACKNOWLEDGEMENTS

We thank Olafur Gudmundsson for providing data from the stations of the Swedish National Seismological Network. MAGNUS waveforms were recorded with the mobile Karlsruhe Broadband Array of the Karlsruhe Institute of Technology (KIT), Germany as well as with permanent stations of the NORSAR array, the Norwegian National Seismological Network and GSN. Continuous data from

the NORSAR array were kindly provided by Johannes Schweitzer. Financial support for the MAGNUS experiment was provided by the Universities of Aarhus, Copenhagen, Karlsruhe and Oslo as well as NORSAR. Seismological stations of the CALAS project, applied in this study, were from the University of Aarhus instrument pool and from the NERC Geophysical Equipment Facility (SEIS-UK). That project was financially supported by the Danish National Science Research Council. Figures have been prepared using the Generic Mapping tools (Wessel *et al.* 2013). We thank two anonymous reviewers for their comments and suggestions that helped to improve this manuscript.

REFERENCES

- Alinaghi, A., Bock, G., Kind, R., Hanka, W. & Wylegalla, K. TOR and SVEKALAPKO Working Groups, 2003. Receiver function analysis of the crust and upper mantle from the North German Basin to the Archaean Baltic Shield, *Geophys. J. Int.*, **155**(2), 641–652.
- Balling, N., 1992. Denmark, in *Geothermal Atlas of Europe*, pp. 25–28, eds Hurlig, E., Cermk, V., Haenel, R. & Zui, V., Hermann Haack, Gotha.
- Balling, N., 1995. Heat flow and thermal structure of the lithosphere across the Baltic Shield and northern Tornquist Zone, *Tectonophysics*, **244**(1), 13–50.
- Barmin, M., Ritzwoller, M. & Levshin, A., 2001. A fast and reliable method for surface wave tomography, *Pure appl. Geophys.*, **158**(8), 1351–1375.
- Bensen, G., Ritzwoller, M., Barmin, M., Levshin, A., Lin, F., Moschetti, M., Shapiro, N. & Yang, Y., 2007. Processing seismic ambient noise data to obtain reliable broad-band surface wave dispersion measurements, *Geophys. J. Int.*, **169**(3), 1239–1260.
- Bingen, B., Andersson, J., Soderlund, U. & Moller, C., 2008a. The Mesoproterozoic in the Nordic countries, *Episodes*, **31**(1), 29.
- Bingen, B., Nordgulen, O. & Viola, G., 2008b. A four-phase model for the Sveconorwegian orogeny, SW Scandinavia, *Norw. J. Geol.*, **88**(1), 43–72.
- Chalmers, J., Green, P., Japsen, P. & Rasmussen, E., 2010. The Scandinavian mountains have not persisted since the Caledonian orogeny. A comment on Nielsen *et al.* (2009a), *J. Geodyn.*, **50**(2), 94–101.
- Cheng, C., Chen, L., Yao, H., Jiang, M. & Wang, B., 2013. Distinct variations of crustal shear wave velocity structure and radial anisotropy beneath the North China Craton and tectonic implications, *Gondwana Res.*, **23**(1), 25–38.
- Cocks, L. & Torsvik, T., 2006. European geography in a global context from the Vendian to the end of the Palaeozoic, *Mem.-Geol. Soc. Lond.*, **32**, 83–95.
- Cotte, N., Pedersen, H. & TOR Working Group, 2002. Sharp contrast in lithospheric structure across the Sorgenfrei-Tornquist Zone as inferred by Rayleigh wave analysis of TOR1 project data, *Tectonophysics*, **360**(1–4), 75–88.
- Dalton, C.A. & Gaherty, J.B., 2013. Seismic anisotropy in the continental crust of northwestern Canada, *Geophys. J. Int.*, **193**(1), 338–348.
- Dunkin, J.W., 1965. Computation of modal solutions in layered, elastic media at high frequencies, *Bull. seism. Soc. Am.*, **55**(2), 335–358.
- Erdman, M.E., Hacker, B.R., Zandt, G. & Seward, G., 2013. Seismic anisotropy of the crust: electron-backscatter diffraction measurements from the Basin and Range, *Geophys. J. Int.*, **195**(2), 1211–1229.
- Eugeno-S Working Group, 1988. Crustal structure and tectonic evolution european of the transition between the Baltic Shield and the North German Caledonides (the EUGENO-S Project), *Tectonophysics*, **150**, 253–348.
- Forsyth, D. & Li, A., 2005. Array analysis of two-dimensional variations in surface wave phase-velocity and azimuthal anisotropy in the presence of multipathing interference, in *Seismic Earth: Array Analysis of Broad-band Seismograms: Geophysical Monograph Series*, Vol. 157, pp. 81–97, American Geophysical Union.
- Frederiksen, S., Nielsen, S.B. & Balling, N., 2001. A numerical dynamic model for the Norwegian–Danish Basin, *Tectonophysics*, **343**(3), 165–183.
- Friederich, W., 1998. Wave-theoretical inversion of teleseismic surface waves in a regional network: phase-velocity maps and a three-dimensional upper-mantle shear-wave-velocity model for southern Germany, *Geophys. J. Int.*, **132**(1), 203–225.
- Gabrielsen, R.H., Braathen, A., Olesen, O., Faleide, J.I., Kyrkjebø, R. & Redfield, T.F., 2005. Vertical movements in south-western Fennoscandia: a discussion of regions and processes from the Present to the Devonian, *Norw. Petrol. Soci. Spec. Publ.*, **12**, 1–28.
- Gee, D.G., Fossen, H., Henriksen, N. & Higgins, A.K., 2008. From the early Paleozoic platforms of Baltica and Laurentia to the Caledonide Orogen of Scandinavia and Greenland, *Episodes*, **31**(1), 44–51.
- Gradmann, S., Ebbing, J. & Fullea, J., 2013. Integrated geophysical modelling of a lateral transition zone in the lithospheric mantle under Norway and Sweden, *Geophys. J. Int.*, **194**(3), 1358–1373.
- Green, P.F., Lidmar-Bergström, K., Japsen, P., Bonow, J.M. & Chalmers, J.A., 2013. Stratigraphic landscape analysis, thermochronology and the episodic development of elevated, passive continental margins, *Geological Survey of Denmark and Greenland (GEUS)*, **30**, 150 pp.
- Gregersen, S., Voss, P., Nielsen, L., Achauer, U., Busche, H., Rabbel, W. & Shomali, Z.H., 2010. Uniqueness of modeling results from teleseismic P-Wave tomography in Project Tor, *Tectonophysics*, **481**(1), 99–107.
- Guo, Z., Gao, X., Wang, W. & Yao, Z., 2012. Upper- and mid-crustal radial anisotropy beneath the central Himalaya and southern Tibet from seismic ambient noise tomography, *Geophys. J. Int.*, **189**(2), 1169–1182.
- Heeremans, M. & Faleide, J.I., 2004. Late Carboniferous-Permian tectonics and magmatic activity in the Skagerrak, Kattegat and the North Sea, *Spec. Publ.—Geol. Soc. Lond.*, **223**, 157–176.
- Hejrani, B., Balling, N., Jacobsen, B.H. & Tilmann, F., 2015. Upper-mantle P- and S-wave velocities across the Northern Tornquist Zone from traveltimes tomography, *Geophys. J. Int.*, in press.
- Hieronymus, C. & Goes, S., 2010. Complex cratonic seismic structure from thermal models of the lithosphere: effects of variations in deep radiogenic heating, *Geophys. J. Int.*, **180**(3), 999–1012.
- Hieronymus, C.F., Shomali, Z.H. & Pedersen, L.B., 2007. A dynamical model for generating sharp seismic velocity contrasts underneath continents: application to the Sorgenfrei–Tornquist Zone, *Earth planet. Sci. Lett.*, **262**(1), 77–91.
- Högdahl, K., Andersson, U.B. & Eklund, O., 2004. The Transscandinavian Igneous Belt (TIB) in Sweden: a review of its character and evolution, *Geol. Surv. Finland, Spec. Paper*, **37**, 1–125.
- Japsen, P. & Chalmers, J., 2000. Neogene uplift and tectonics around the North Atlantic: overview, *Glob. Planet. Change*, **24**(3–4), 165–173.
- Kennett, B., Engdahl, E. & Buland, R., 1995. Constraints on seismic velocities in the earth from travel-times, *Geophys. J. Int.*, **122**(1), 108–124.
- Knudsen, H.J., Balling, N. & Jacobsen, B.H., 1991. Seismic modelling of the Norwegian–Danish basin along a refraction profile in northern Jutland, *Tectonophysics*, **189**(1), 209–218.
- Köhler, A., Weidle, C. & Maupin, V., 2011. Directionality analysis and Rayleigh wave tomography of ambient seismic noise in southern Norway, *Geophys. J. Int.*, **184**, 287–300.
- Köhler, A., Weidle, C. & Maupin, V., 2012. Crustal and uppermost mantle structure of southern Norway: results from surface wave analysis of ambient noise and earthquake data, *Geophys. J. Int.*, **191**, 1441–1456.
- Kolstrup, M.L., Hung, S.-H. & Maupin, V., 2015. Multiscale, finite-frequency P and S tomography of the upper mantle in the southwestern Fennoscandian Shield, *Geophys. J. Int.*, **202**(1), 190–218.
- Lahtinen, R., Garde, A.A. & Melezhik, V.A., 2008. Paleoproterozoic evolution of Fennoscandia and Greenland, *Episodes*, **31**(1), 20.
- Lee, C.-T.A., 2003. Compositional variation of density and seismic velocities in natural peridotites at STP conditions: implications for seismic imaging of compositional heterogeneities in the upper mantle, *J. geophys. Res.: Solid Earth*, **108**(B9), 2441, doi:10.1029/2003JB002413.
- Levshin, A., Yanovskaya, T., Lander, A., Bukchin, B., Barmin, M., Ratnikova, L. & Its, E., 1989. *Seismic Surface Waves in a Laterally Inhomogeneous Earth*, ed. Keilis-Borok, V.I., Kluwer, Norwell, MA.
- Lin, F.-C., Moschetti, M.P. & Ritzwoller, M.H., 2008. Surface wave tomography of the western united states from ambient seismic noise: Rayleigh and love wave phase-velocity maps, *Geophys. J. Int.*, **173**(1), 281–298.

- Maupin, V., 1985. Partial derivatives of surface-wave phase velocities for flat anisotropic models, *Geophys. J. R. astr. Soc.*, **83**(2), 379–398.
- Maupin, V., 2011. Upper-mantle structure in southern Norway from beam-forming of Rayleigh wave data presenting multipathing, *Geophys. J. Int.*, **185**, 985–1002.
- Maupin, V. & Park, J., 2007. Theory and observations—wave propagation in anisotropic media, in *Treatise on Geophysics*, Vol. 1: *Seismology and the Structure of the Earth*, pp. 289–321, eds Romanowicz, B. & Dziewonski, A., Elsevier, Boston.
- Maupin, V. *et al.*, 2013. The deep structure of the Scandes and its relation to tectonic history and present-day topography, *Tectonophysics*, **602**, 15–37.
- Medhus, A., Balling, N., Jacobsen, B., Weidle, C., England, R., Kind, R., Thybo, H. & Voss, P., 2012. Upper-mantle structure beneath the Southern Scandes Mountains and the Northern Tornquist Zone revealed by P-wave traveltimes tomography, *Geophys. J. Int.*, **189**(3), 1315–1334.
- Moschetti, M., Ritzwoller, M., Lin, F. & Yang, Y., 2010a. Seismic evidence for widespread western-US deep-crustal deformation caused by extension, *Nature*, **464**(7290), 885–889.
- Moschetti, M., Ritzwoller, M., Lin, F. & Yang, Y., 2010b. Crustal shear wave velocity structure of the western United States inferred from ambient seismic noise and earthquake data, *J. geophys. Res.*, **115**(B10), B10306, doi:10.1029/2010JB007448.
- Nielsen, S. *et al.*, 2009. The evolution of western Scandinavian topography: A review of Neogene uplift versus the ICE (isostasy-climate-erosion) hypothesis, *J. Geodyn.*, **47**(2–3), 72–95.
- Nielsen, S., Clausen, O., Jacobsen, B.H., Thomsen, E., Huuse, M., Gallagher, K., Balling, N. & Egholm, D., 2010. The ICE hypothesis stands: How the dogma of late Cenozoic tectonic uplift can no longer be sustained in the light of data and physical laws, *J. Geodyn.*, **50**(2), 102–111.
- Pedersen, H., Campillo, M. & Balling, N., 1994. Changes in the lithospheric structure across the Sorgenfrei-Tornquist Zone inferred from dispersion of Rayleigh waves, *Earth planet. Sci. Lett.*, **128**(1), 37–46.
- Prindle, K. & Tanimoto, T., 2006. Teleseismic surface wave study for S-wave velocity structure under an array: Southern California, *Geophys. J. Int.*, **166**(2), 601–621.
- Rickers, F., Fichtner, A. & Trampert, J., 2013. The Iceland–Jan Mayen plume system and its impact on mantle dynamics in the North Atlantic region: evidence from full-waveform inversion, *Earth planet. Sci. Lett.*, **367**, 39–51.
- Ritzwoller, M. & Levshin, A., 1998. Eurasian surface wave tomography: group velocities, *J. geophys. Res.*, **103**, 4839–4878.
- Roberts, D., 2003. The Scandinavian Caledonides: event chronology, palaeogeographic settings and likely modern analogues, *Tectonophysics*, **365**(1), 283–299.
- Sabra, K., Gerstoft, P., Roux, P., Kuperman, W. & Fehler, M., 2005. Extracting time-domain Green's function estimates from ambient seismic noise, *Geophys. Res. Lett.*, **32**, L03310, doi:10.1029/2004GL021862.
- Saito, M., 1988. DISPER80: A subroutine package for the calculation of seismic normal-mode solutions, in *Seismological Algorithms: Computational Methods and Computer Programs*, pp. 293–319, ed. Doornbos, D.J., Academic Press, New York.
- Sambridge, M., 1999. Geophysical inversion with a neighbourhood algorithm—I. searching a parameter space, *Geophys. J. Int.*, **138**(2), 479–494.
- Sandrin, A. & Thybo, H., 2008. Deep seismic investigation of crustal extensional structures in the Danish Basin along the ESTRID-2 profile, *Geophys. J. Int.*, **173**(2), 623–641.
- Schutt, D.L. & Leshner, C.E., 2010. Compositional trends among Kaapvaal Craton garnet peridotite xenoliths and their effects on seismic velocity and density, *Earth planet. Sci. Lett.*, **300**(3), 367–373.
- Seats, K.J., Lawrence, J.F. & Prieto, G.A., 2012. Improved ambient noise correlation functions using Welch's method, *Geophys. J. Int.*, **188**(2), 513–523.
- Shapiro, N. & Campillo, M., 2004. Emergence of broadband Rayleigh waves from correlations of the ambient seismic noise, *Geophys. Res. Lett.*, **31**(7), 1615–1619.
- Slagstad, T., Balling, N., Elvebakk, H., Midtømme, K., Olesen, O., Olsen, L. & Pascal, C., 2009. Heat-flow measurements in Late Palaeoproterozoic to Permian geological provinces in south and central Norway and a new heat-flow map of Fennoscandia and the Norwegian–Greenland Sea, *Tectonophysics*, **473**(3), 341–361.
- Smirnov, M.Y. & Pedersen, L.B., 2009. Magnetotelluric measurements across the Sorgenfrei-Tornquist Zone in southern Sweden and Denmark, *Geophys. J. Int.*, **176**(2), 443–456.
- Stratford, W. & Thybo, H., 2011. Seismic structure and composition of the crust beneath the southern Scandes, Norway, *Tectonophysics*, **502**(3–4), 364–382.
- Stratford, W., Thybo, H., Faleide, J., Olesen, O. & Tryggvason, A., 2009. New Moho Map for onshore southern Norway, *Geophys. J. Int.*, **178**(3), 1755–1765.
- Svenningsen, L., Balling, N., Jacobsen, B., Kind, R., Wylegalla, K. & Schweitzer, J., 2007. Crustal root beneath the highlands of southern Norway resolved by teleseismic receiver functions, *Geophys. J. Int.*, **170**(3), 1129–1138.
- Tarantola, A. & Valette, B., 1982. Generalized nonlinear inverse problems solved using the least squares criterion, *Rev. Geophys. Space Phys.*, **20**(2), 219–232.
- Thybo, H., 2001. Crustal structure along the EGT profile across the Tornquist Fan interpreted from seismic, gravity and magnetic data, *Tectonophysics*, **334**(3), 155–190.
- Torsvik, T.H. & Cocks, L.R.M., 2005. Norway in space and time: a Centennial calvalcade, *Norw. J. Geol.*, **85**(1–2), 73–86.
- Torsvik, T.H., Smethurst, M.A., Burke, K. & Steinberger, B., 2008. Long term stability in deep mantle structure: evidence from the ~300 Ma Skagerrak-Centered Large Igneous Province (the SCLIP), *Earth planet. Sci. Lett.*, **267**(3), 444–452.
- Valcke, S.L.A., Casey, M., Lloyd, G.E., Kendall, J.M. & Fisher, Q.J., 2006. Lattice preferred orientation and seismic anisotropy in sedimentary rocks, *Geophys. J. Int.*, **166**(2), 652–666.
- Wathelet, M., 2008. An improved neighborhood algorithm: parameter conditions and dynamic scaling, *Geophys. Res. Lett.*, **35**(9), L09301, doi:10.1029/2008GL033256.
- Wathelet, M., Jongmans, D. & Ohrnberger, M., 2004. Surface wave inversion using a direct search algorithm and its application to ambient vibration measurements, *Near Surf. Geophys.*, **2**(4), 211–221.
- Wawerzinek, B., Ritter, J.R.R. & Roy, C., 2013. New constraints on the 3D shear wave velocity structure of the upper mantle underneath Southern Scandinavia revealed from non-linear tomography, *Tectonophysics*, **602**(SI), 38–54.
- Weidle, C., 2012. Surface wave phase-velocity maps from multiscale wave field interpolation, *Comput. Geosci.*, **16**(3), 535–549.
- Weidle, C. *et al.*, 2010. MAGNUS—A seismological broadband experiment to resolve crustal and upper mantle structure beneath the southern Scandes mountains in Norway, *Seism. Res. Lett.*, **81**(1), 76–84.
- Weiss, T., Siegesmund, S., Rabbel, W., Bohlen, T. & Pohl, M., 1999. Seismic velocities and anisotropy of the lower continental crust: a review, *Pure appl. Geophys.*, **156**(1–2), 97–122.
- Wessel, P., Smith, W., Scharroo, R., Luis, J. & Wobbe, F., 2013. Generic mapping tools: improved version released, *EOS, Trans. Am. geophys. Un.*, **94**(45), 409–410.
- Yang, Y., Shen, W. & Ritzwoller, M., 2011. Surface wave tomography on a large-scale seismic array combining ambient noise and teleseismic earthquake data, *Earthq. Sci.*, **24**(1), 55–64.
- Yao, H., Beghein, C. & Van Der Hilst, R., 2008. Surface wave array tomography in SE Tibet from ambient seismic noise and two-station analysis—II. Crustal and upper-mantle structure, *Geophys. J. Int.*, **173**(1), 205–219.

APPENDIX: EARTHQUAKE DATA AND PHASE-VELOCITY MEASUREMENTS

The number of phase-velocity measurements available is quite variable for the different subnetworks, periods and wave types (Figs A13 and A14). In general, we have twice as much data for Rayleigh waves

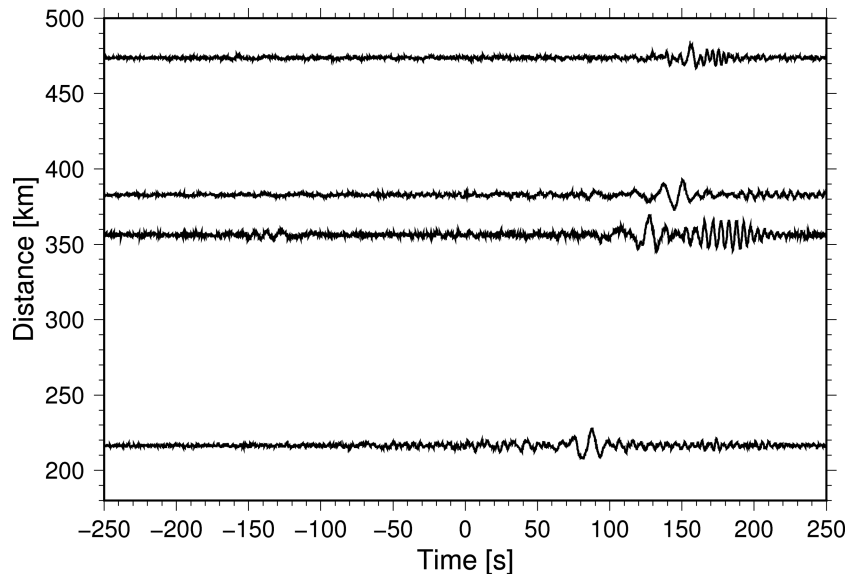


Figure A1. Examples of empirical Green's functions for stations pairs MUD-COP, MUD-KONO, MUD-BSD and COP-KONO (from bottom to top).

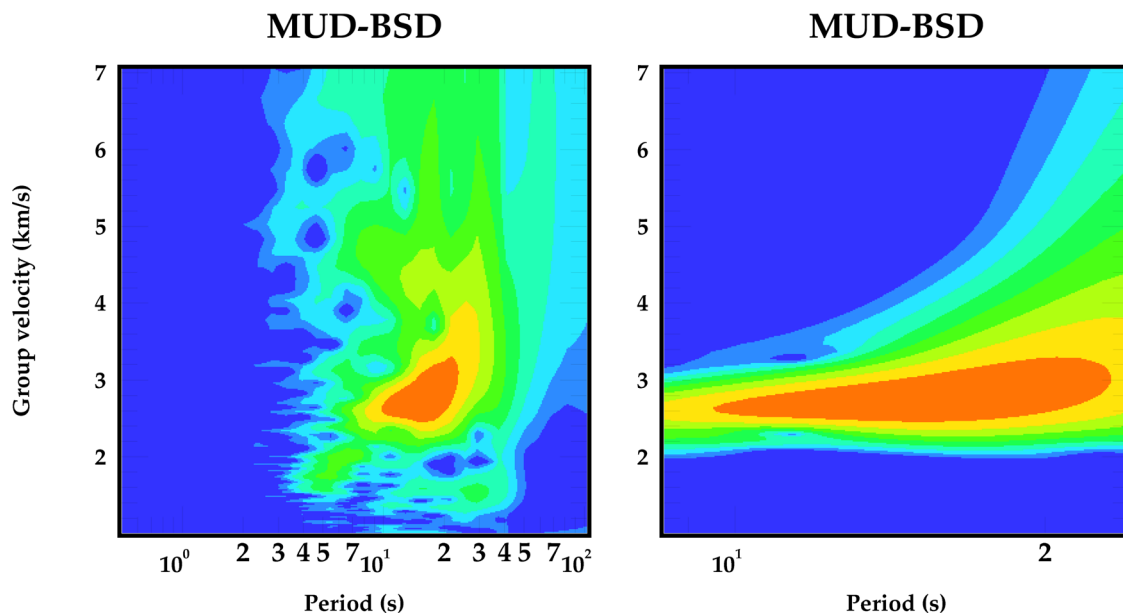


Figure A2. Example FTAN image of raw and cleaned signal for station pair MUD-BSD (vertical component).

than for Love waves. The NOR subnetwork consists of a rather homogeneous set of broad-band stations that were operating simultaneously during the MAGNUS experiment (Weidle *et al.* 2010), leading to a good exploitation of the event database at this subnetwork. In addition, there is no major difference between the amount of data passing the selection criteria at the different stations and each station contributes quite equally to the final dispersion curve. The DEN subnetwork is more heterogeneous. The three stations on the Norwegian coast and the two permanent stations COP and MUD contribute with more data than the other temporary stations, especially at periods longer than 40 s. These five major stations delineate an area to the west and the final curve at longer periods could be slightly biased toward the structure in this area. Some stations in the middle of the SWE subnetwork have little overlap

in time with the other stations or have been installed for a shorter time period. The average number of data contributed by each station at the different periods is similar to what we have at the DEN subnetwork if all events are taken into account, but reduced due to the backazimuth restriction we have imposed. We are however fortunate to have permanent stations COP and BSD in the south and permanent station HFC2 and two stations of the MAGNUS network in the north which contribute with much data, giving all together a sufficient data basis and a good geographical coverage of the area. The Swedish National Seismological Network (SNSN) has now several additional permanent stations in the area but they did not operate simultaneously with the temporary stations used here and could not be used to expand the database.

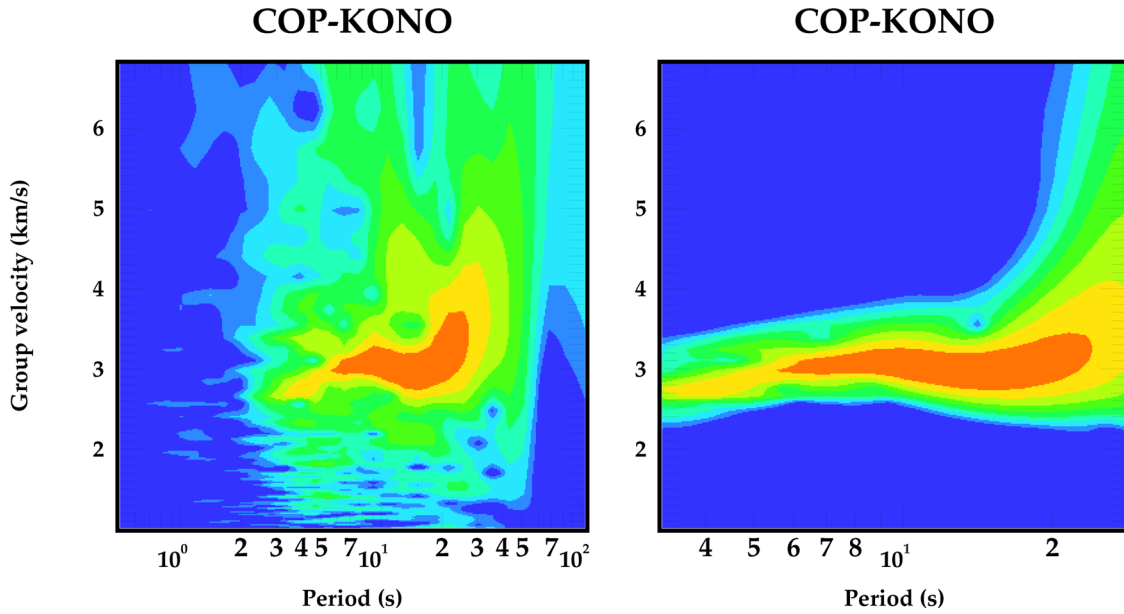


Figure A3. Example FTAN image of raw and cleaned signal for station pair COP-KONO (vertical component).

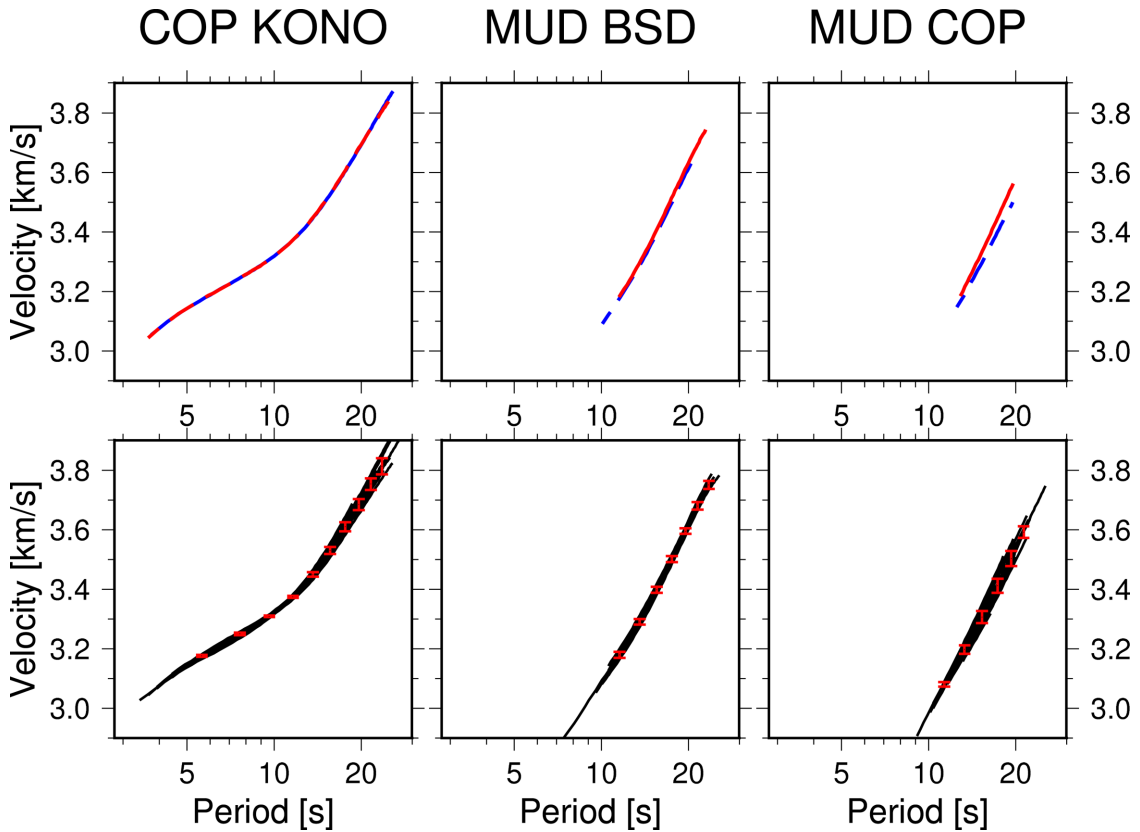


Figure A4. Prove of stability of Rayleigh wave phase-velocity dispersion curves. Upper panels: velocities measured from NCF stack of summer (red) and winter months (blue). Lower panels: velocities measured with one month overlapping stacks of three months (black). Mean and standard deviation (red).

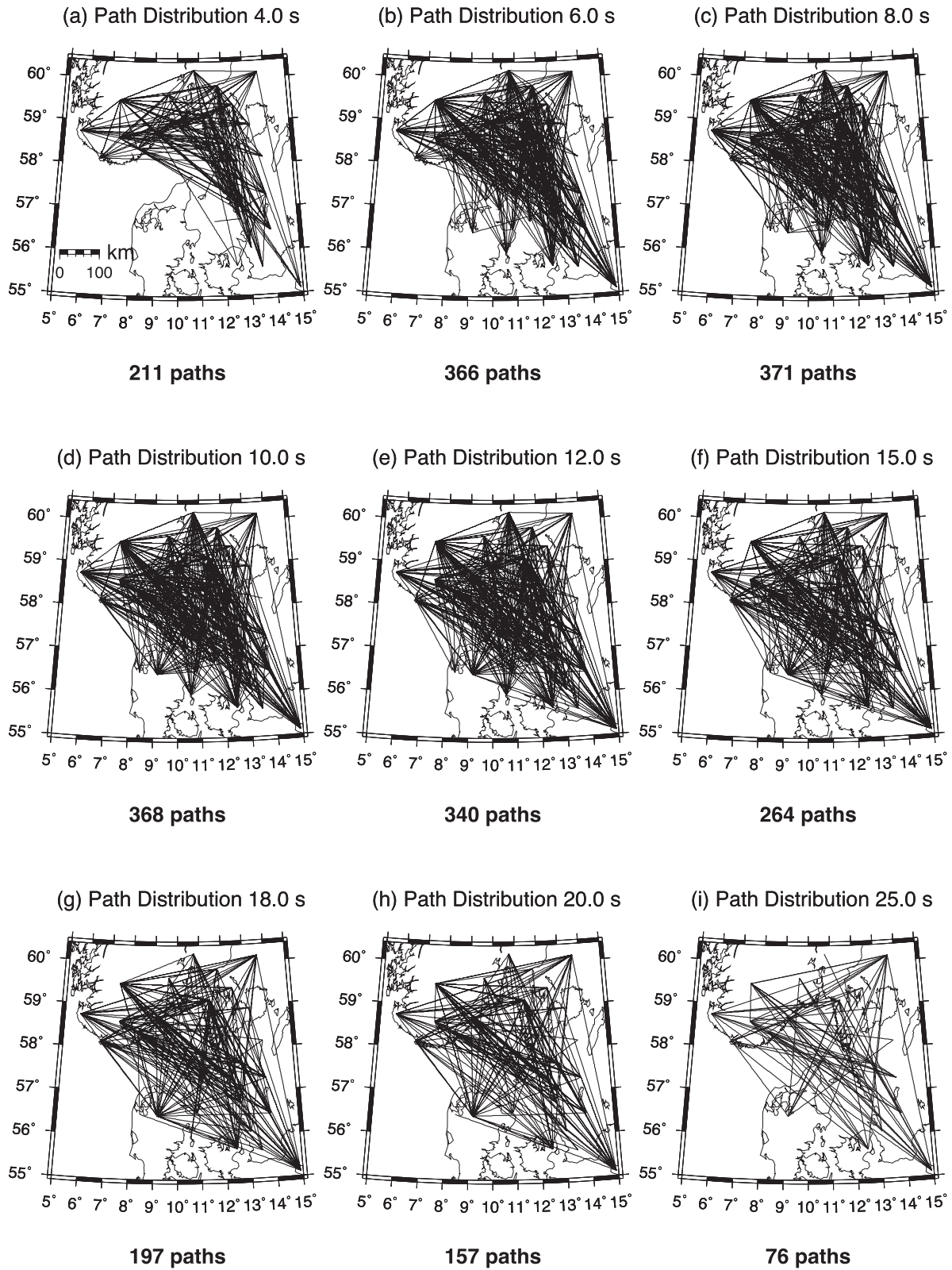


Figure A5. Path distribution for inversion of Rayleigh wave phase-velocity maps.

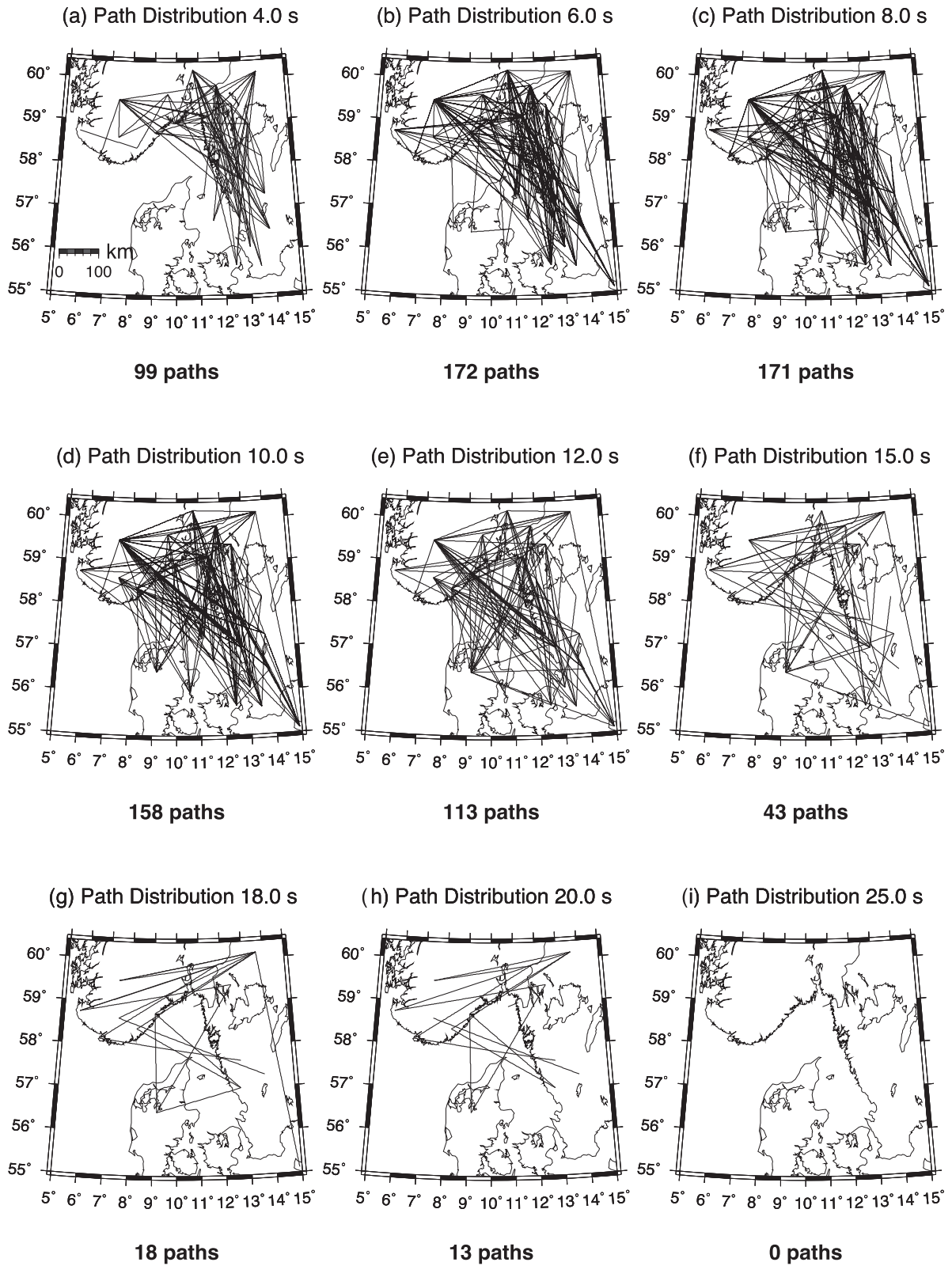


Figure A6. Path distribution for inversion of Love wave phase-velocity maps.

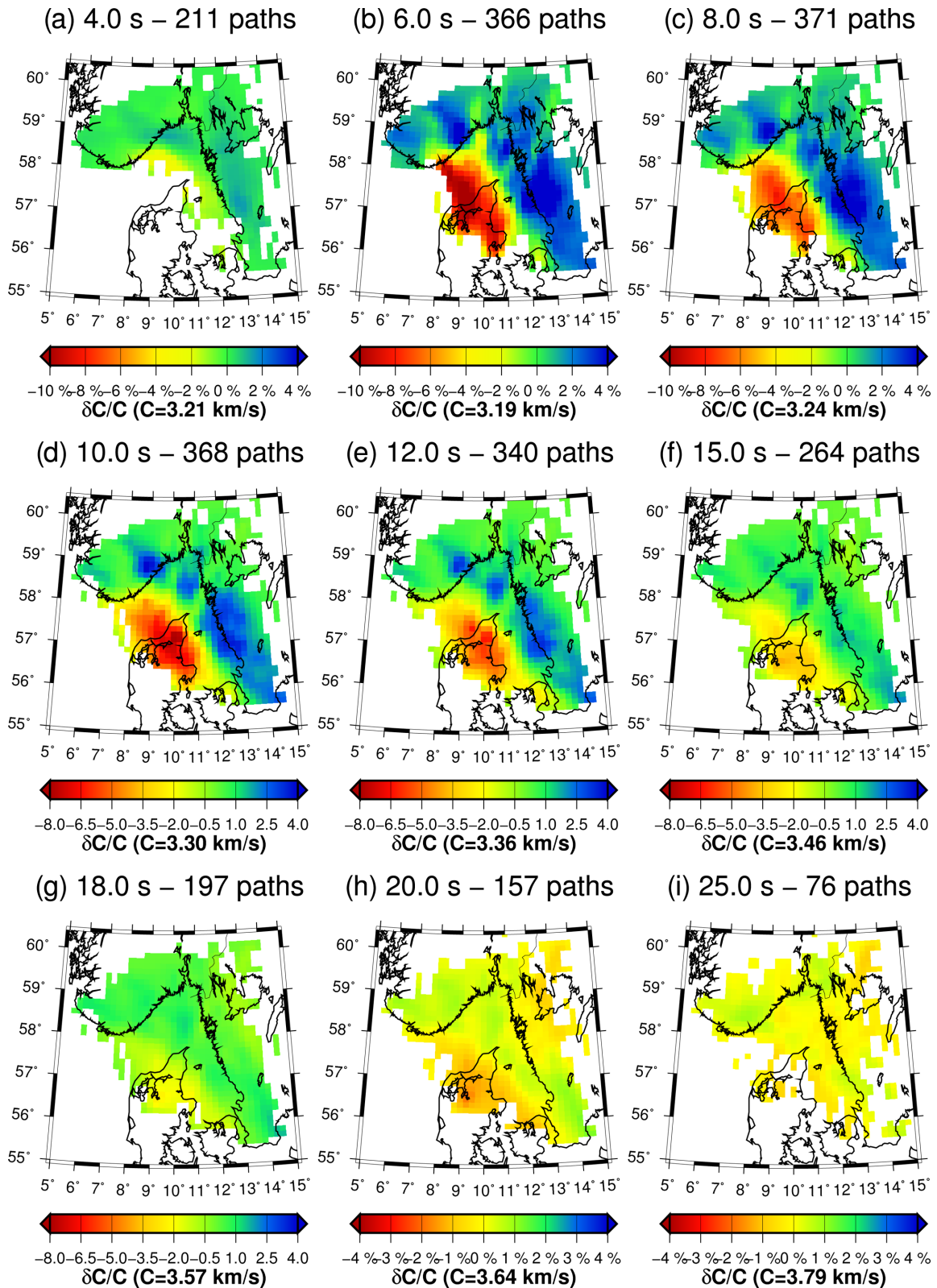


Figure A7. Rayleigh wave phase-velocity maps.

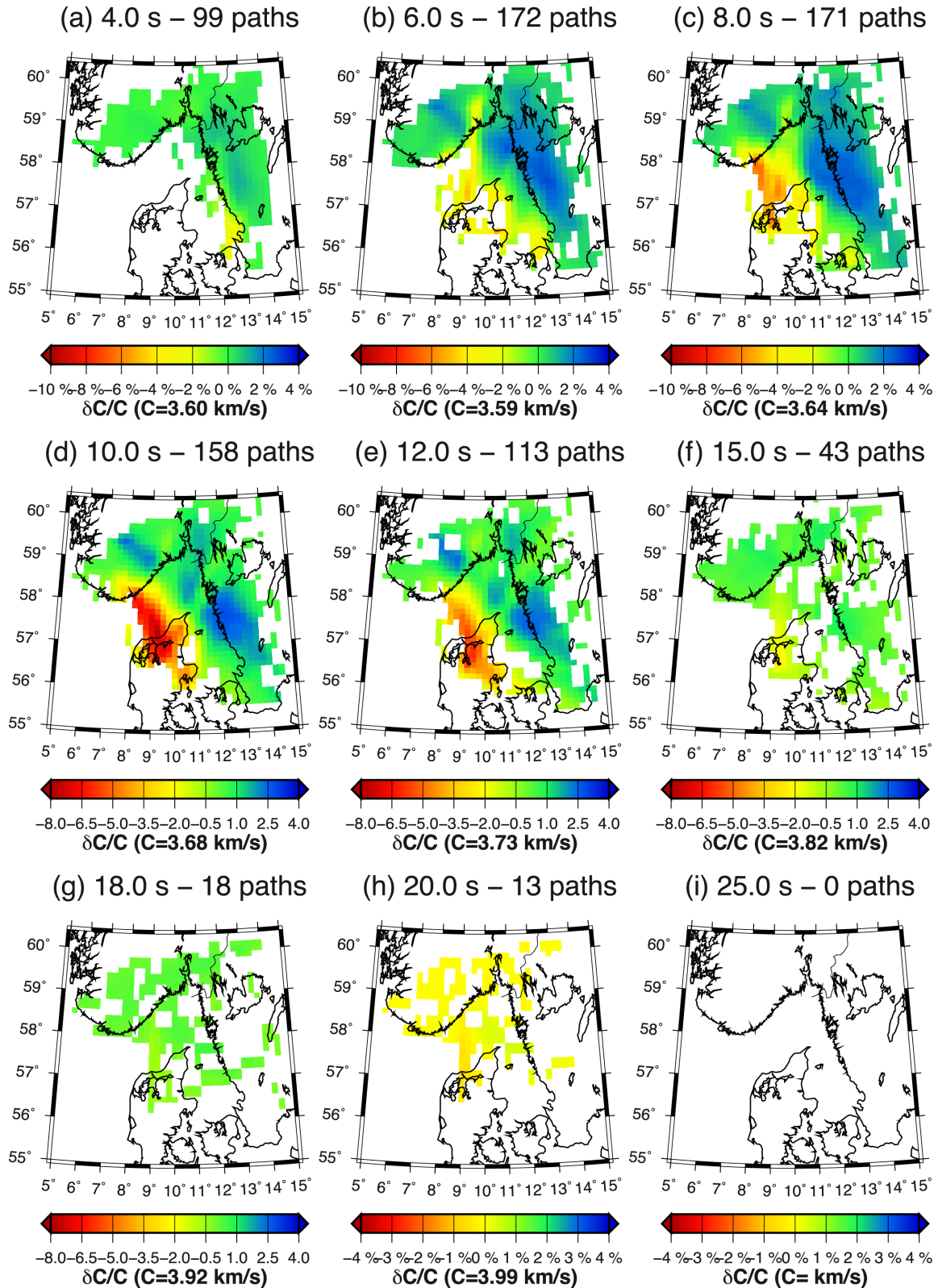


Figure A8. Love wave phase-velocity maps.

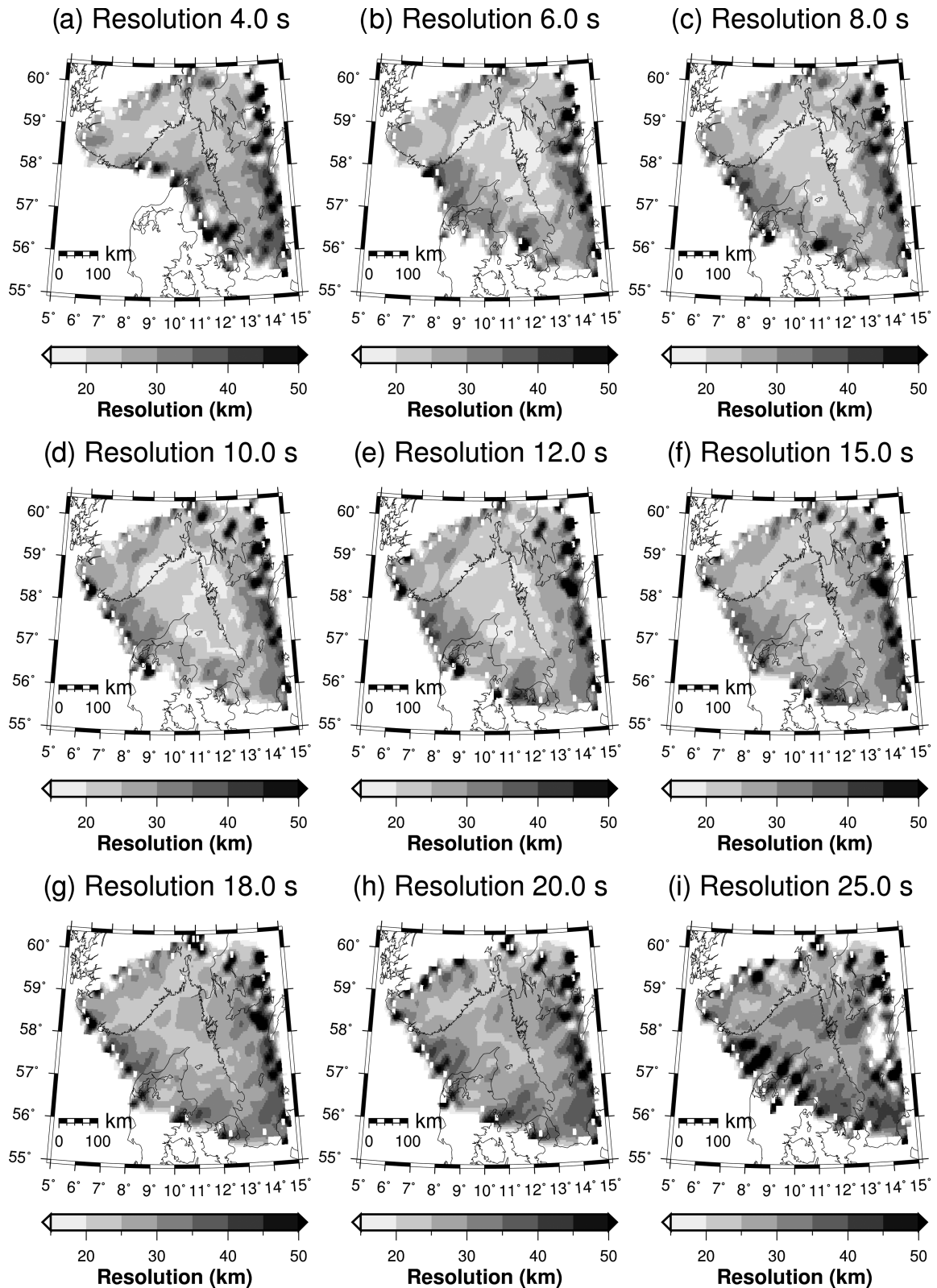


Figure A9. Resolution of Rayleigh wave phase velocities obtained using the method of Barmin *et al.* (2001).

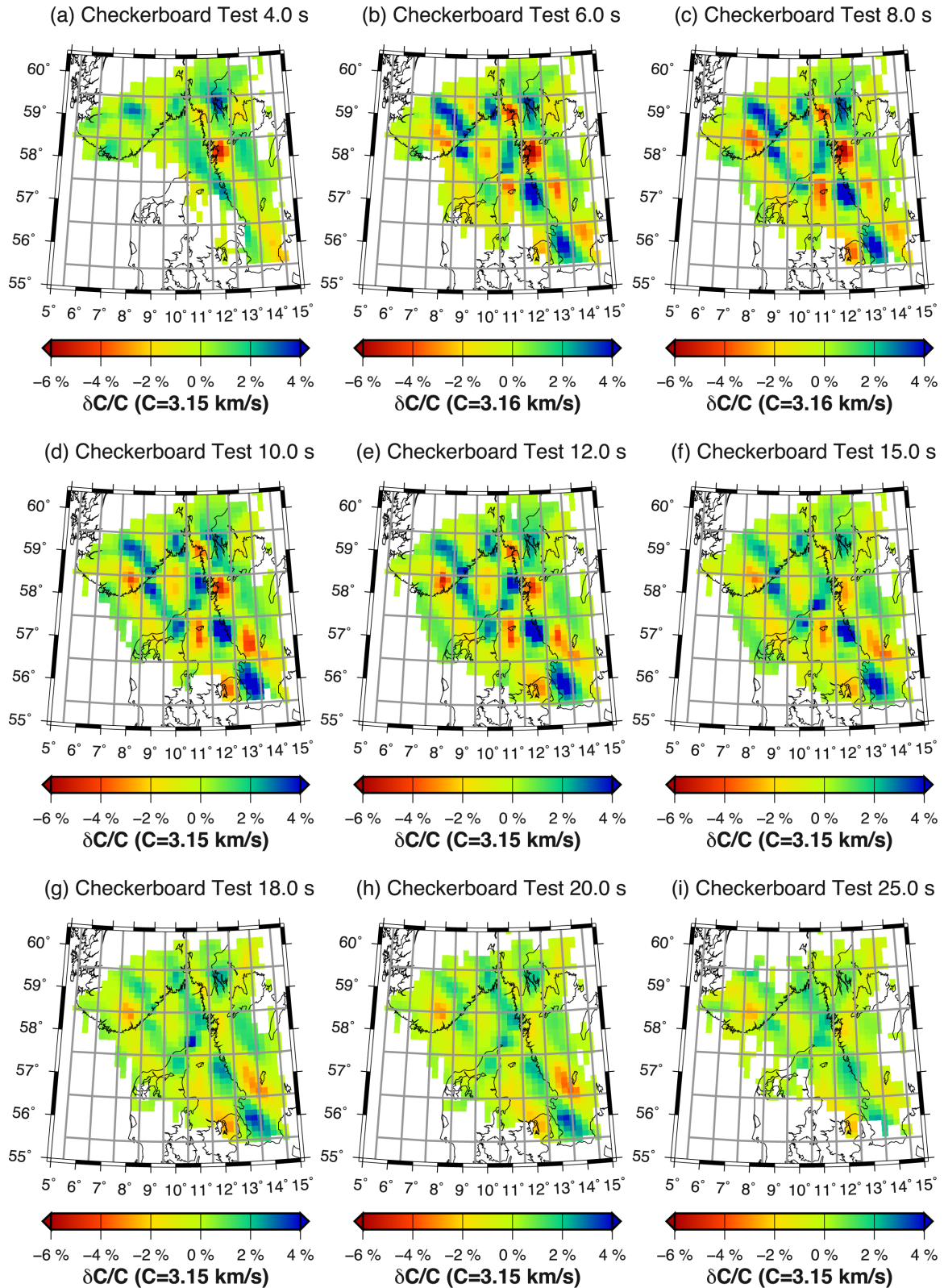


Figure A10. Result of a checkerboard test for phase-velocity tomography. Synthetic velocity anomalies are -11.7 per cent and 5 per cent (alternating distribution in grey rectangular).

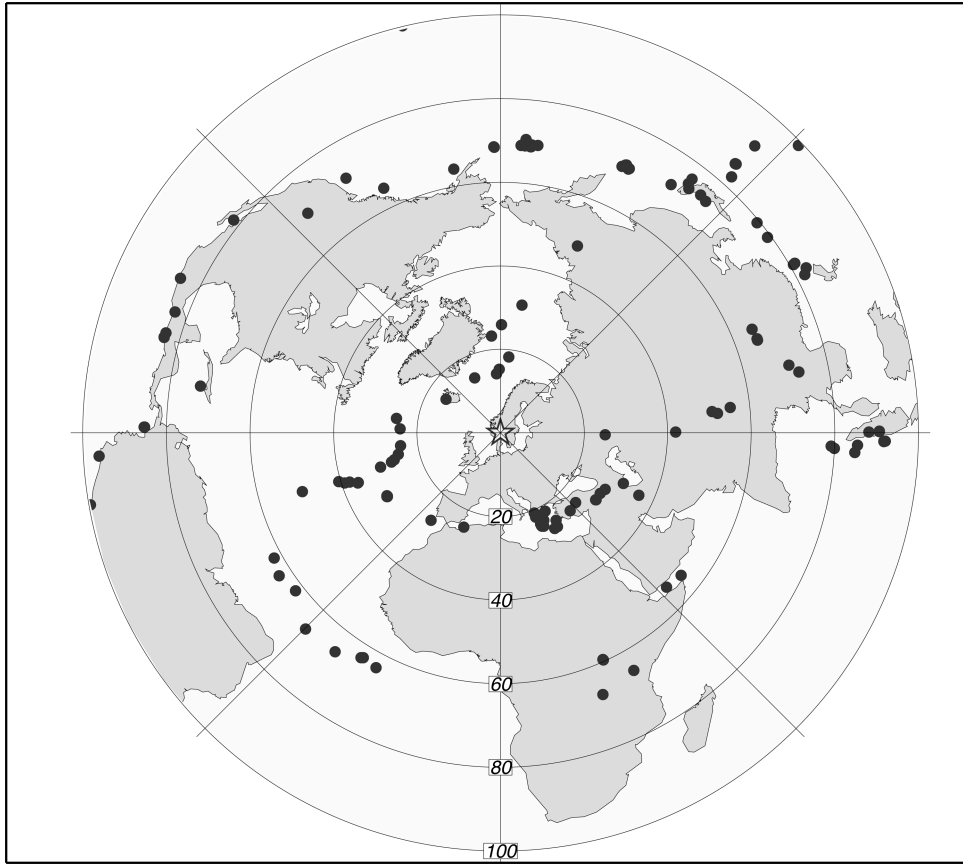


Figure A11. Distribution of seismic events used in this study.

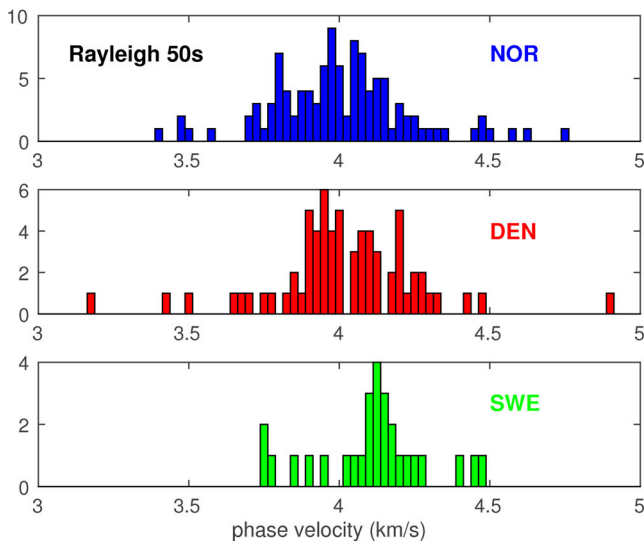
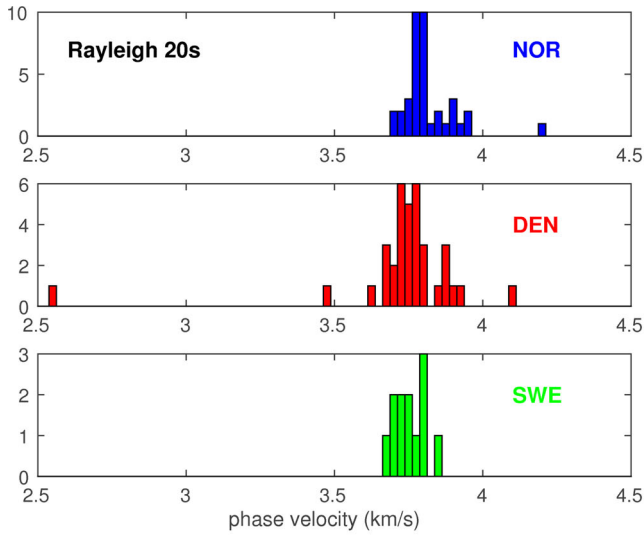


Figure A12. Distribution of phase velocities measured with earthquake data for 20 and 50 s period.

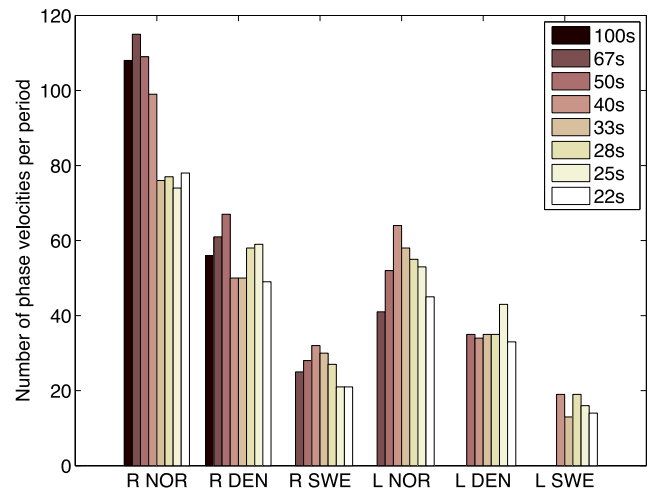


Figure A13. Number of phase velocities measured with earthquake data in the period range 22–100 s for the three subnetworks.

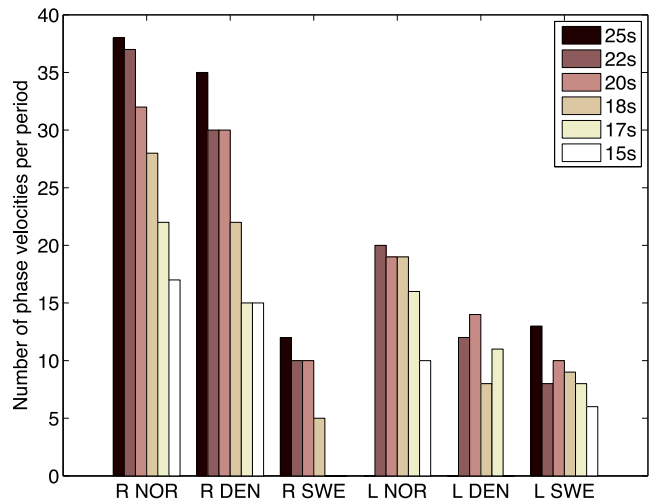


Figure A14. Number of phase velocities measured with earthquake regional data in the period range 15–25 s for the three subnetworks.